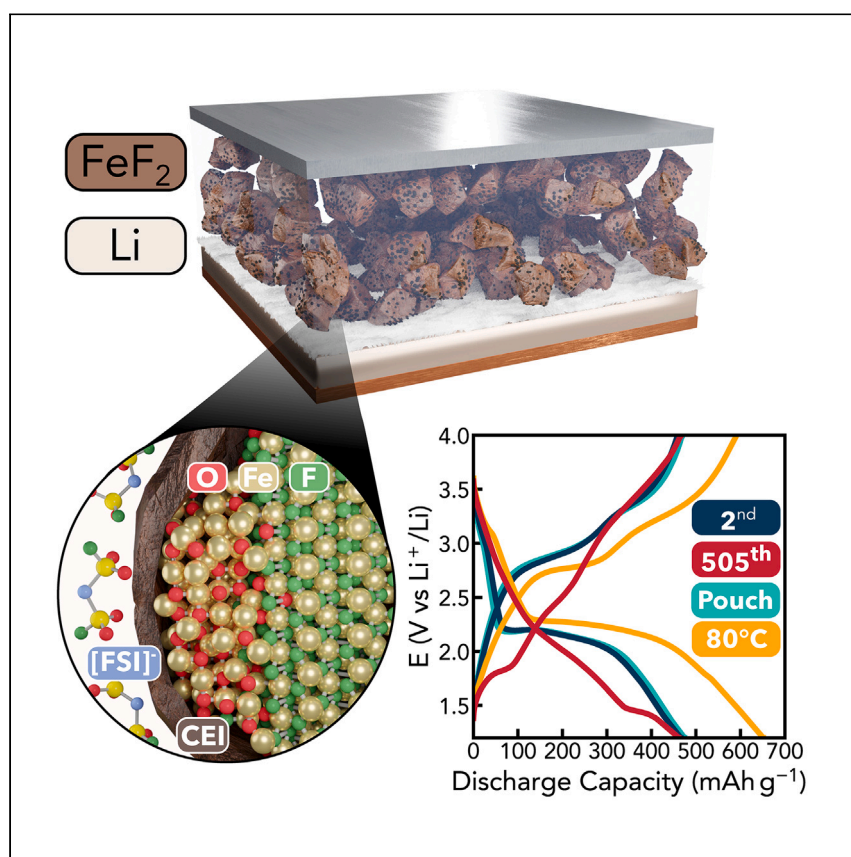


## Article

# Iron fluoride-lithium metal batteries in bis(fluorosulfonyl)imide-based ionic liquid electrolytes



Olbrich et al. explored the iron fluoride-lithium metal system with an FSI-based ionic liquid electrolyte, finding that FSI prevents particle agglomeration but is consumed in a degradation mechanism forming iron oxide. The authors examine its viability for electric flight applications.

Lorenz F. Olbrich, Albert W. Xiao, Maximilian Schart, Johannes Ihli, Guillaume Matthews, Mohan Sanghadasa, Mauro Pasta

mauro.pasta@materials.ox.ac.uk

### Highlights

Wet-milling conditions for homogeneous iron fluoride particle size distribution

Composite cathode with an active material content of 85% by novel mixing technique

FSI anion creates a protective interphase, prevents particle fusion, yet depletes with cycling

Reversible cycling using a metallic lithium anode up to 120°C

Olbrich et al., Cell Reports Physical Science 5, 101787

February 21, 2024 © 2024 The Authors.

<https://doi.org/10.1016/j.xcrp.2024.101787>



## Article

## Iron fluoride-lithium metal batteries in bis(fluorosulfonyl)imide-based ionic liquid electrolytes

Lorenz F. Olbrich,<sup>1</sup> Albert W. Xiao,<sup>1</sup> Maximilian Schart,<sup>1</sup> Johannes Ihli,<sup>1</sup> Guillaume Matthews,<sup>1</sup> Mohan Sanghadasa,<sup>2</sup> and Mauro Pasta<sup>1,3,\*</sup>

## SUMMARY

The aviation industry's shift toward electrification demands greater energy density and enhanced cell safety compared to commercial lithium-ion batteries. Transition metal fluoride cathodes can store multiple lithium ions per metal center through a conversion reaction mechanism, resulting in a 3-fold increase in capacity compared to intercalation compounds. Additionally, fluoride cathodes exhibit remarkable thermal stability due to the ionic nature of the metal-fluoride bond. However, their practical implementation faces challenges due to their limited electronic and ionic conductivity. In this study, we conducted a comprehensive investigation of FeF<sub>2</sub>-Li metal cells in a lithium bis(fluorosulfonyl)imide *N*-propyl-*N*-methylpyrrolidinium bis(fluorosulfonyl)imide ionic liquid electrolyte. We explored the effects of FeF<sub>2</sub> particle size, the distribution of conductive additives within the electrode, and the influence of the bis(fluorosulfonyl)imide anion on electrochemical behavior and its evolution throughout cycling. Our findings suggest that the rate requirements for electric aviation could be met at 80°C.

## INTRODUCTION

The aviation industry is responsible for more than 2% of the world's energy-related carbon dioxide emissions. Although it is among the fastest-growing sources of emissions, it is also one of the most challenging sectors to decarbonize.<sup>1</sup> Electrification of aerospace transport is critical in order to meet climate targets, yet thus far this has only been commercially realized in small drones.<sup>2</sup> The next step in the development of viable electric flights is short-range (up to 400 km) transport in urban environments using electric (vertical) take-off and landing aircraft.<sup>2,3</sup> The key challenges toward realizing these aircraft are demanding battery requirements including higher energy densities, improved cell safety, and a rate capability able to meet the high discharge currents required during take-off and landing.<sup>2,4–8</sup>

Realizing a significant step increase in energy density requires next-generation cathode chemistries, particularly as battery energy density is cathode limited.<sup>2</sup> Transition metal fluoride (TMF) cathodes are one of the leading cathode chemistry contenders, since they can store multiple Li ions per metal center due to a conversion reaction mechanism and thus increase the theoretical energy density by 200%–300% compared to intercalation compounds.<sup>9–11</sup> In addition, TMF cathodes exhibit excellent thermal stability up to approximately 1,000°C and consist of low-cost and abundant elements such as iron.<sup>10,12–15</sup>

<sup>1</sup>Department of Materials, University of Oxford, Parks Road, Oxford OX1 3PH, UK

<sup>2</sup>U.S. Army Combat Capabilities Development Command Aviation & Missile Center, Redstone Arsenal, AL 35898, USA

<sup>3</sup>Lead contact

\*Correspondence: [mauro.pasta@materials.ox.ac.uk](mailto:mauro.pasta@materials.ox.ac.uk)  
<https://doi.org/10.1016/j.xcrp.2024.101787>



Extensive mechanistic studies have advanced our understanding of the conversion reaction in TMF cathodes over the last 20 years.<sup>16–25</sup> For example, it was found that a stable fluoride anion host structure is maintained during lithiation and delithiation of  $\text{FeF}_x$ , revealing a high intrinsic cycling reversibility.<sup>26–28</sup> Unfortunately, the same fluoride anion host structure exhibits a wide band gap resulting in sluggish charge-carrier conductivities.<sup>17,25</sup> Impractical amounts of conductive additives (>50 wt %) are typically used to achieve stable cycling and to access the full capacity of  $\text{FeF}_2$  at reasonable current densities.<sup>29–36</sup> From a techno-economic perspective, this dilution of the active material renders TMFs noncompetitive with the next generation of intercalation cathodes due to a reduction in practical energy density.<sup>10</sup> To address this limitation, various active material preparation techniques have been explored to produce TMF nanostructures and minimize diffusion lengths. However, most of these techniques are not suitable for producing active material at scale.<sup>27,37,38</sup> Ball milling is a desirable processing technique that allows for high throughput, minimal waste production, and the use of commercially available materials. However, reports on ball-milled TMF cathodes in the literature typically show fewer than ten cycles at extremely slow cycling rates.<sup>16,39</sup>

Here, we present a systematic investigation of ball-milled  $\text{FeF}_2$  cathodes in a lithium bis(fluorosulfonyl)imide *N*-propyl-*N*-methylpyrrolidinium bis(fluorosulfonyl)imide ( $\text{LiFSI Pyr}_{1,3}\text{FSI}$ ) ionic liquid (IL) electrolyte and demonstrate stable capacity retention for over 500 cycles. We provide a holistic framework linking particle size, electronic conductivity, and the role of bis(fluorosulfonyl)imide ( $[\text{FSI}]^-$ ) anions to its electrochemical cycling behavior. The thermal stability of our electrolyte, combined with a cell construction amenable to high-temperature operation enables us to demonstrate reversible cycling up to 120°C. Lastly, we show that power requirements for electric aviation applications could be met at elevated temperatures.

## RESULTS AND DISCUSSION

### Wet-milling strategies for improved performance

To access the full capacity of TMF cathodes despite the short ionic and electronic diffusion lengths in metal fluorides, nanosizing of the active material is required. Ball milling is arguably the most scalable processing technique to decrease and control particle size. Inspired by standard milling conditions reported in the literature, our initial experiments involved “dry” ball milling of commercial  $\text{FeF}_2$  powder.<sup>16</sup> Unfortunately, this resulted in a wide particle size distribution and insufficient particle size reduction due to coarsening caused by the local heating generated in the process (Figure S1).<sup>40,41</sup> To overcome this limitation, octadecene, a high-boiling solvent, was added to the mixture. This “wet” milling technique prevented the adhesion of  $\text{FeF}_2$  to the milling surfaces, lowered the impact, and increased the shear forces generated by the milling process.<sup>40,41</sup> In addition, we added small amounts of oleic acid as a surfactant to the mixture to maintain a colloidal dispersion of separate particles throughout the milling.<sup>27</sup>

Dynamic light scattering (DLS) was used to track the particle size distribution profiles of wet-milled  $\text{FeF}_2$ . Figure 1A compares the median particle sizes and the width of distribution as a function of milling time for three different ball-milling speeds (500, 700, and 900 rpm). The D90 and D10 values indicate the average diameter for the 90<sup>th</sup> and 10<sup>th</sup> percentile, respectively, that is, 80% of particles in the sample, are sized between the D90 and D10 values. In all cases, particle sizes decreased steadily with milling time up to 8 h, maintaining a monomodal distribution (Figure S2). After 12 h of milling, a slight increase in the D90 values can be observed,

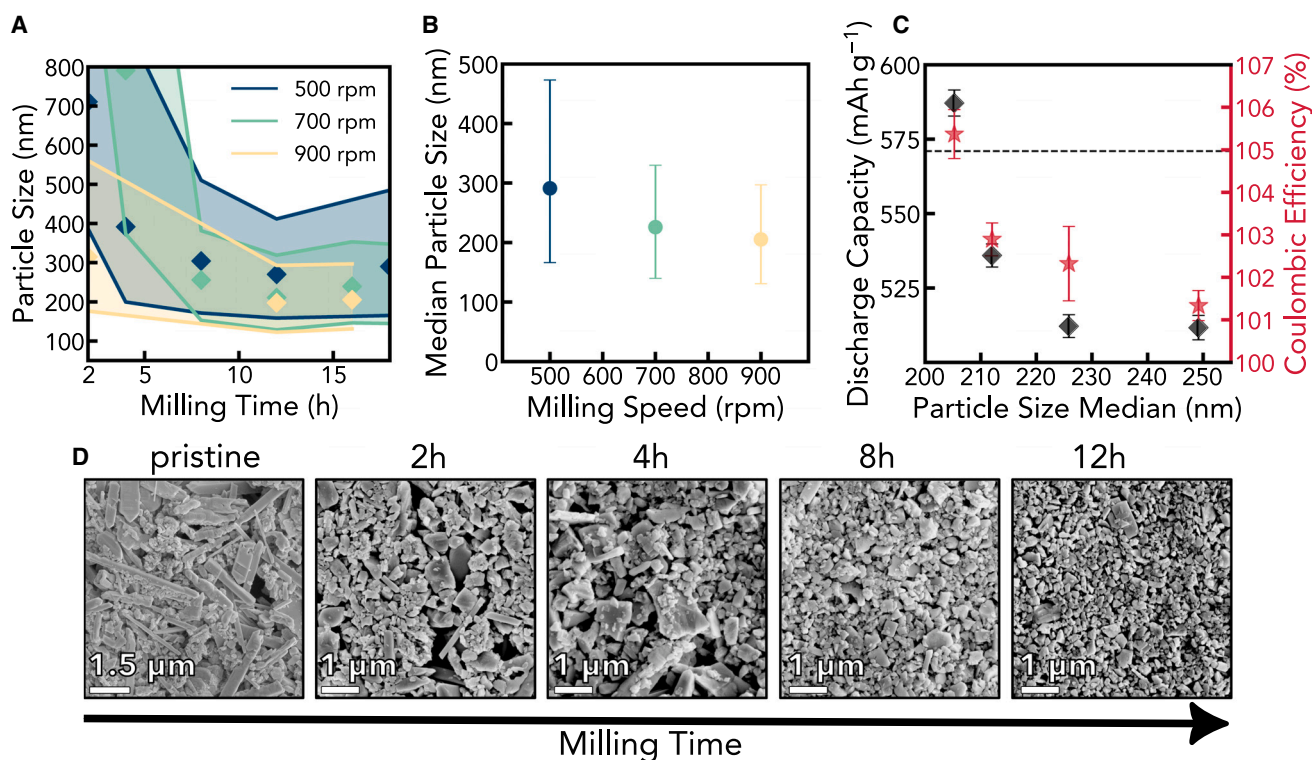


**Figure 1. Wet-milling strategies for improved performance**

(A) D10 to D90 of  $\text{FeF}_2$  particles determined by DLS as a function of milling time at different rotation speeds. The diamond-shaped dots inside the plot indicate respective particle median.

(B) Median (final)  $\text{FeF}_2$  particle size as a function of rpm. The error bars correspond to the respective D10 to D90 values.

(C) Average discharge capacity (black) and Coulombic efficiency (red) with standard deviation of  $\text{FeF}_2$  prepared under different ball-milling conditions and evaluated in a coin cell using a 1 M LiFSI  $\text{Pyr}_{1.3}$ FSI electrolyte and a lithium metal anode. Cells were cycled at C/20 at 30°C. The dotted line corresponds to the theoretical capacity of  $\text{FeF}_2$ .

(D) SEM images of  $\text{FeF}_2$  particle aliquots extracted from a wet-milling process (700 rpm) at increasing milling times.

which might be due to particle coarsening facilitated by the generated heat. A similar trend was observed in an earlier study on  $\text{FeF}_3$ -carbon composites.<sup>16</sup> To prevent a further particle size increase in the 900-rpm run, the synthesis was stopped after 16 h. The final particle size as a function of milling speed is plotted in Figure 1B. The maximum size reduction and narrowest particle size distribution are achieved with increased rotation speeds.

Particle size quantification using scanning electron microscopy (SEM) images in Figure 1D (see Figure S3 for a statistical analysis) corroborates the determined size profile by DLS. Post-milling electron diffraction micrographs of selected particles prove that the milling process produces single crystals (Figure S4). This is critical, since a stable fluoride anion host structure has been identified as a key enabler for the high cycling reversibility of  $\text{FeF}_2$  cathodes.<sup>26–28</sup> The novel solvent-surfactant-based wet-milling recipe demonstrated here enables an improved control of the particle size range and benign processing conditions, resulting in single-crystalline active material. The recipe can be transferred to other TMF cathodes, resulting in an equally small average particle size and narrow size distribution, as shown in Figure S5.

To test the effect of particle size on the electrochemical properties of milled  $\text{FeF}_2$ , electrodes from different milling batches were prepared using the co-dispersion



method described in “[comparative analysis of carbon mixing techniques](#).” The cathodes were tested in a coin-cell configuration with a lithium metal counter electrode and filled with a 1 M LiFSI Pyr<sub>1,3</sub>FSI IL electrolyte. The IL electrolyte has demonstrated beneficial electrochemical properties for reversible FeF<sub>2</sub> cycling in earlier studies due to the formation of a stable cathode electrolyte interphase (CEI) and compatibility with lithium metal anodes.<sup>27,42–44</sup>

The average discharge capacity and Coulombic efficiency (CE) at the third cycle at C/20 are compared and depicted as a function of particle diameter median in [Figure 1C](#). The data suggest that a smaller particle diameter leads to an increase in accessible discharge capacity and CE. The poor ionic and electronic conductivity of FeF<sub>2</sub> can explain the lower accessible capacity in larger particles, as the inner particle core becomes isolated if the particles exceed the diffusion length of lithium ions and electrons.<sup>16,19,29,45</sup> Ko and colleagues determined a lithium diffusion coefficient of around  $1 \times 10^{-18} \text{ cm}^2 \text{ s}^{-1}$  in FeF<sub>2</sub> and suggested that particle sizes below 20 nm are required to achieve a complete conversion reaction. Nanoparticles of that size commonly demand laborious and unscalable synthesis techniques (e.g., solution and colloidal synthesis or direct fluorination<sup>27,30,45–47</sup>) and catalyze parasitic electrolyte reactions.<sup>10</sup> Other studies demonstrated capacities above  $500 \text{ mA h}^{-1}$  in single crystals (around 200 nm long) and measured significantly larger diffusion coefficients.<sup>26,27,48,49</sup> Here, we report that a particle median of around 200 nm is sufficiently small to access the theoretical capacity ( $571 \text{ mA h}^{-1}$ ) of ball-milled, single-crystalline FeF<sub>2</sub> particles at slow cycling rates (C/20) and 30°C.

### Comparative analysis of carbon mixing techniques

For practical applications, cathodes need to operate at higher current densities while keeping overpotentials and dilution by conductive additives low to enable high energy densities. This can be achieved by ensuring that the active material is well dispersed and in good contact with the conductive additive. In this section, conventional and novel FeF<sub>2</sub>-carbon black mixing techniques are characterized and compared to optimize practical power and energy densities.

- Mortar and pestle (MP): a conventional lab-scale mixing technique whereby the active material and the carbon black were thoroughly ground with a mortar and pestle.
- Co-dispersion (CD): a meta-stable dispersion of both the active material and the carbon black was prepared in separate solvents, mixed, and centrifuged to remove the liquid phase.
- Ultra-stirring (US): a novel technique combining CD with additional ultrasonication (20% amplitude sonication and continuous stirring for 1 h in 1,2-dichloroethane) to further improve the mixing by breaking up clusters or aggregates of material.

Electrodes were fabricated from the different composites with an active material content of 70 wt %. The cathodes were wet cast and calendered to a thickness of 15  $\mu\text{m}$  using identical amounts of composite and solvent, resulting in reproducible areal capacities of around  $1.5 \text{ mg cm}^{-2}$ . Powder X-ray diffraction (XRD) patterns of cathodes from all three composites show clear diffraction peaks, indicating that the process of creating the composite did not affect the crystallinity of the active material ([Figure S6](#)).

The particle morphology in each electrode was imaged and compared in top-view ([Figure S7](#)) and cross-sectional geometry, shown in [Figures 2A and S8](#)). The SEM

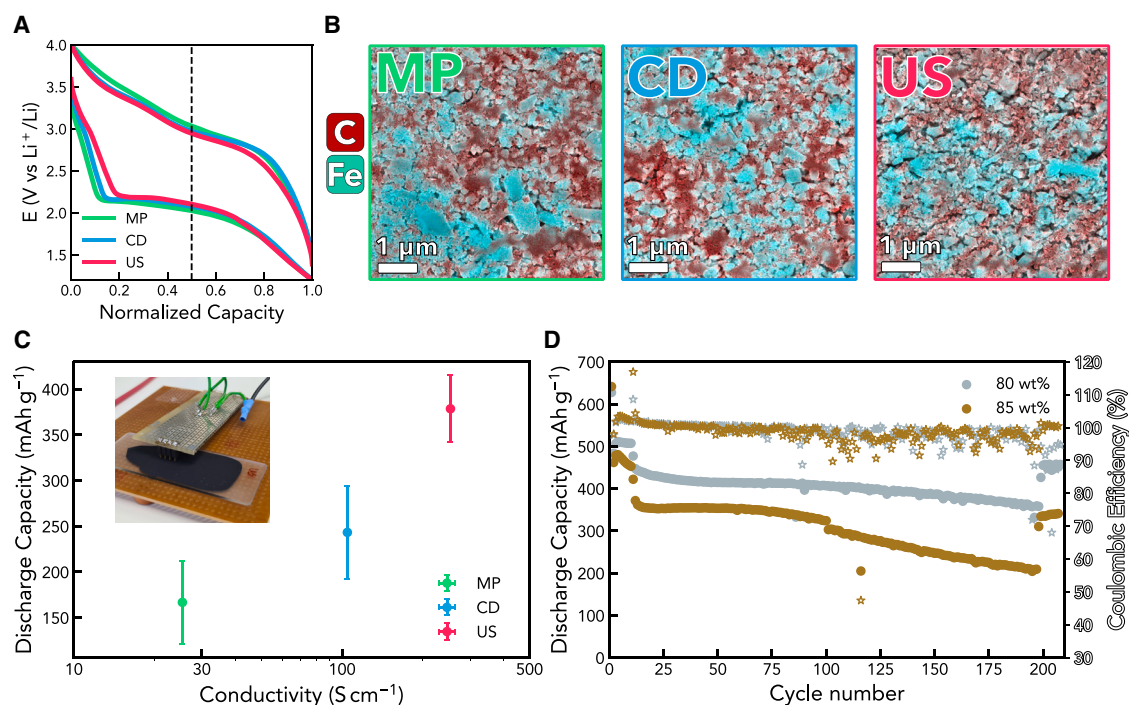


**Figure 2. Comparative analysis of carbon mixing techniques**

(A) GCPL of three different composites, mortar and pestle (MP), co-dispersion (CD), and ultra-stirring (US), at the third cycle in a 1 M LiFSI Pyr<sub>1,3</sub>FSI electrolyte at 30°C.

(B) Composite cathode cross-sections prepared by broad-beam argon milling tool (Gatan Precision Etching Coating System). Energy-dispersive X-ray spectroscopy was used to map carbon and iron.

(C) Average cathode discharge capacity and standard deviation at cycle number 50 (C/5) as a function of conductivity measured by a four-probe setup. The setup is shown in the inset photo.

(D) Discharge capacity (dots) and Coulombic efficiency (stars) as a function of cycle number of US FeF<sub>2</sub> cathodes with 80 wt % and 85 wt % active material content in a 1 M LiFSI Pyr<sub>1,3</sub>FSI electrolyte at 30°C.

images show that the active material morphology remains unchanged during the composite preparation, corroborating the benign conditions during the composite preparation. Occasional larger particles are found in all three composites. These larger particles originated from incomplete size reduction during milling, as depicted in Figure 1B. Elemental mapping of MP and CD indicates carbon agglomeration between the FeF<sub>2</sub> particles, while the US composite exhibits a more homogeneous carbon distribution.

Galvanostatic cycling with potential limitation (GCPL) was conducted at a low rate of C/20 (approximately 35 μA cm<sup>-2</sup>) to test the cycling performance of the electrodes prepared with the three different techniques. The normalized potential profiles of the third cycles are plotted in Figure 2B.

The profiles are very similar, with slightly higher potential observed in the US cathodes. The voltage hysteresis, defined here as the differences of the recharge and discharge potential at 50% state-of-charge (SOC), is reduced from 1.01 V to 0.89 V and down to 0.84 V for the MP, CD, and US cathode, respectively, suggesting an improved electronic conductivity in the US composite. Similarly, at the 100<sup>th</sup> cycle at a C/5 rate, the hysteresis follows the same trend (MP, 1.39 V; CD, 1.19 V; US, 1.03 V) as shown in Figure S9. The discharge capacity as a function of cycle number is shown in Figure S10.

To further quantify the effectiveness of the carbon mixing techniques, the composites were wet cast onto an insulating glass substrate, and their electronic conductivity was measured using a Van der Pauw four-probe setup. Figure 2C shows the conductivity of the composites and their corresponding discharge capacities at a cycling rate of C/5 at cycle number 50. A higher discharge capacity can be obtained with cathodes that exhibit high conductivity. While the energy-dispersive X-ray spectroscopy (EDX) cross-sections of the MP and CD castings showed a very similar carbon distribution, the conductivity of the latter was almost an order of magnitude larger. This suggests that CD improves carbon distribution compared to mechanical grinding (MP). When mixing the two dispersions during CD, the carbon particles aggregate onto the  $\text{FeF}_2$  surface to minimize the interfacial energy, resulting in a more homogeneous carbon distribution. Correspondingly, the discharge capacity of CD cathodes is almost  $100 \text{ mA h g}^{-1}$  higher than in MP.

The highest conductivity was found for the US casting, which aligns well with the most homogeneous carbon distribution observed in the cross-section. While the CD relies on a single aggregation event of active material and carbon, the US allows continuous aggregation and redispersion throughout the mixing, which further improves the carbon distribution and, consequently, the electronic conductivity.

Considering that the active material particles are of identical size in different composites, i.e., the lithium diffusion lengths are identical, and the accessible capacity increases with electronic conductivity, we conclude that electronic transport in the composite is the limiting factor over ionic conductivity in the investigated system. Furthermore, the capacity retention in Figure S6 suggests that the distribution of super p on the active material affects the cycling reversibility. Electrolyte decomposition is expected to occur along electronic pathways in the composite and thus affects the homogeneity of the CEI.

As described in our previous techno-economic analysis,<sup>10</sup> a high discharge capacity with an active material mass fraction closer to 85% is required to produce a cell with a competitive energy density. This has not been achieved to date due to the low electronic conductivity of TMF cathodes. Using the US composite preparation technique, we prepared  $\text{FeF}_2$  electrodes with active material mass fractions between 70% and 85%, as shown in Figures 2D, S11, and S12. The 70% cell was able to deliver the full discharge capacity over more than 500 cycles. The 80 wt % and 85 wt % cells exhibit near theoretical capacities with no discernible difference in capacity retention at slow cycling rates (C/20) and maintained 90% and 72% capacity over 220 cycles. The high capacity retention in US  $\text{FeF}_2$  cathodes at such a high active material content marks the best cycling performance reported for TMF cathodes to date (Figure S13). The CE of the cells stabilizes at around 100.6% until roughly the 100<sup>th</sup> cycle when CEs below 100% are measured. Further characterization of the cycled electrodes was conducted to investigate the origin of parasitic reactions causing the decay in CE.

### Aging mechanisms and morphological evolution during cycling

A CE of 101.77% and 99.26% were measured on the second and the 505<sup>th</sup> cycle of a US cathode, respectively.  $\text{FeF}_2$  commonly exhibits excess discharge capacity during the first cycle, resulting in CE above 100% due to the formation of a CEI. The CEI formation is further facilitated by the catalytic activity of the metal phase formed during discharge, and as a result a CE above 100% is characteristic for TMF cathodes.<sup>10,27,44</sup> However, a drop below 100% is indicative of parasitic reactions occurring with progressing cycling.

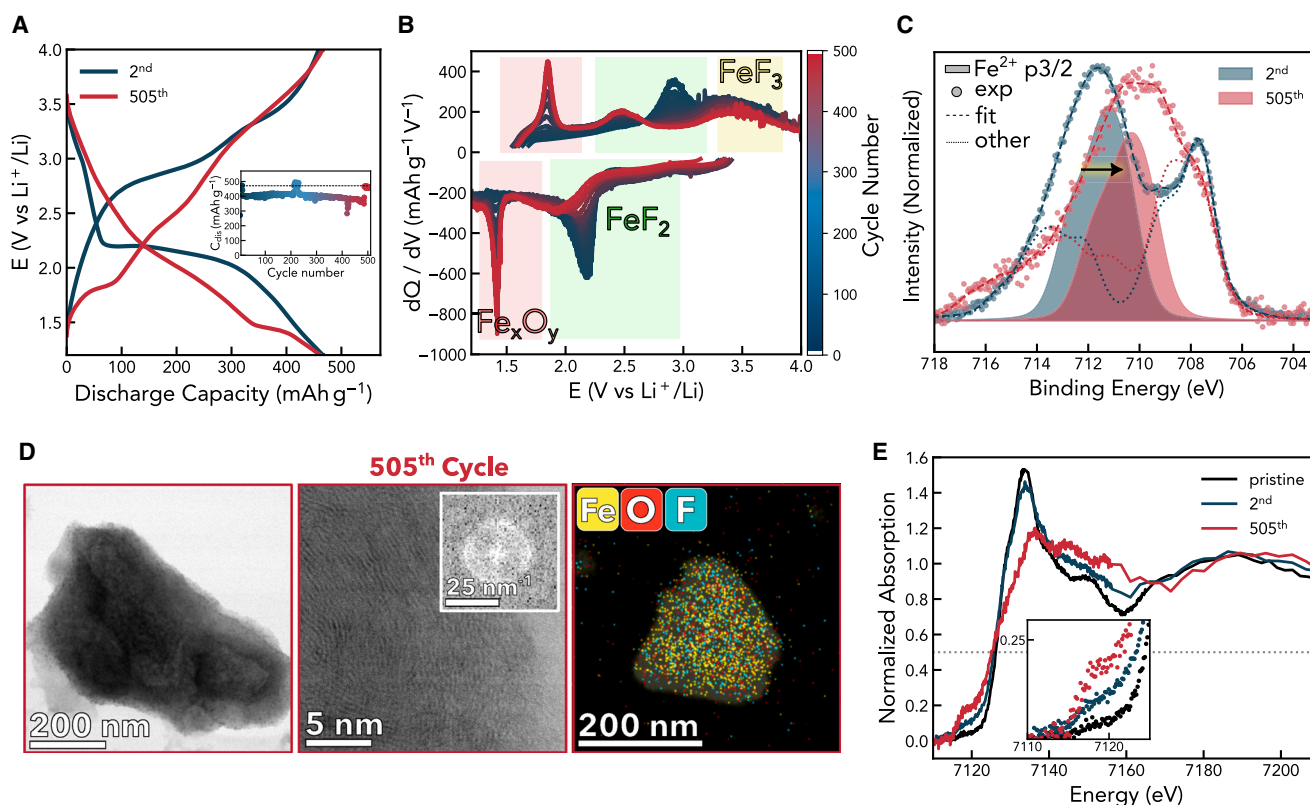


**Figure 3. Aging mechanisms and morphological evolution during cycling**

(A) GCPL of an ultra-stirred FeF<sub>2</sub>-IL lithium metal cell after 2 and 505 cycles at 30°C.

(B) Corresponding differential capacity plot highlighting different redox processes occurring at different potentials (yellow for FeF<sub>3</sub>; green for FeF<sub>2</sub>; red for Fe<sub>x</sub>O<sub>y</sub>).

(C) XPS of iron highlighting the Fe<sup>2+</sup> p<sub>3/2</sub> peak position after 2 and 505 cycles, respectively.

(D) TEM, STEM, and EDX images of the active material particles after 505 cycles.

(E) Fe K-edge XANES measurement of the cycled cathodes in comparison to a pristine FeF<sub>2</sub> cathode.

To better understand the electrochemical cycling behavior, the GCPL of the second and 505<sup>th</sup> cycle and the evolution of differential capacity (dQ/dV) are plotted in Figures 3A and 3B, respectively. A discharge capacity of 461 mA h g<sup>-1</sup> is maintained over more than 500 cycles (1% capacity fading), which corresponds to 81.5% of the theoretical capacity of FeF<sub>2</sub>. However, the voltage profiles exhibit different features, which indicate a change in redox reactions. The main voltage plateau located at 2.25 V vs. Li<sup>+</sup>/Li and 2.8 V vs. Li<sup>+</sup>/Li in the second discharge and recharge cycle gradually shifts to lower potentials (marked green in the dQ/dV plot). At the same time, the plateau-specific voltage hysteresis, defined as the voltage distance of the respective dQ/dV peaks, shrinks from 731 mV to 552 mV over 500 cycles. Consequently, the plateau shift to a lower potential is not a result of a growing overpotential.

Additionally, the GCPL at cycle 505 shows a capacity of around 100 mA h g<sup>-1</sup> over 2.5 V vs. Li<sup>+</sup>/Li during discharge and recharge. The increased potential can be ascribed to the occurrence of Fe<sup>3+</sup>-Fe<sup>2+</sup> redox reactions and has previously been reported.<sup>27</sup> Moreover, an additional reduction and oxidation plateau emerges at 350 mA h g<sup>-1</sup> to 450 mA h g<sup>-1</sup> and 0 mA h g<sup>-1</sup> to 100 mA h g<sup>-1</sup> during cell discharge and recharge at 1.45 V and 1.85 V vs. Li<sup>+</sup>/Li, respectively. The dQ/dV plot clearly shows

its gradual occurrence after about 250 cycles (red box). The evolution of this additional redox feature at low potentials suggests the gradual formation of a new redox-active species during cycling (Figure S14). It is noteworthy that the redox plateau was also observed in cells cycled inside an argon-filled glovebox. A plausible reversible redox couple that could be formed at this potential is  $\text{Fe}_2\text{O}_3$  or  $\text{Fe}_3\text{O}_4$ . Indeed, both iron oxides exhibit an initial lithiation potential of around 1.4 V, which aligns well with the observed reduction potential in the GCPL.<sup>16,50–52</sup> The formation of an  $\text{Fe}_3\text{O}_4$  surface layer on  $\text{FeF}_2$  has been previously reported.<sup>53</sup>

To further elucidate the aging mechanism of  $\text{FeF}_2$  cathodes, the cycled cell was disassembled at 100% SOC, analyzed, and compared to an identical cathode that was only cycled twice. X-ray photoelectron spectroscopy (XPS) was used to characterize the chemical composition and binding environment of the active material in the cathodes. Around 20% of metallic iron can be detected in both cathodes, as shown in the complete XPS profile in Figure S15. Isolation of metallic iron trapped in a disordered surface layer of the active material, irreversible capacity loss, and the formation of  $\text{Fe}^{3+}$  has been previously observed by Xiao et al. in the first cycle of  $\text{FeF}_2$  cathodes.<sup>27</sup> Both capacity above 2.5 V vs.  $\text{Li}^+/\text{Li}$  which is indicative of  $\text{Fe}^{3+}$  redox and a capacity below the theoretical value of  $\text{FeF}_2$  are observed in Figure 3A, in agreement with the detection of metallic iron in the presented XPS results.

In Figure 3C the Fe  $p_{3/2}$  energy range is shown for the cathode after 505 cycles and an identical cell after two cycles. Spectra were calibrated using the carbon peak located at 284.8 eV and sputtered for 1 h with argon ions to remove the CEI and thus increase the iron signal. For simplicity, only the  $\text{Fe}^{2+}$   $p_{3/2}$  fits are shown. A complete fit of all components can be found in Figures S15 and S16.<sup>54</sup> Interestingly, a shift of the  $\text{Fe}^{2+}$   $p_{3/2}$  peak from 710.7 to 709.6 eV can be observed. Both peaks align with reported values for  $\text{FeF}_2$  and  $\text{Fe}_2\text{O}_3$  or  $\text{Fe}_3\text{O}_4$ , respectively.<sup>54</sup> This further corroborates the formation of an  $\text{Fe}^{3+}$  oxide species during cycling.

To collect further information on the morphology and elemental composition of the active material, the cathode was washed and redispersed in *N*-methyl-2-pyrrolidone to remove the binder and electrolyte decomposition products. Scanning transmission electron microscopy (STEM) and transmission electron microscopy (TEM) micrographs (Figure 3D) after cycling display primary active material particle size in the 250–400 nm range, which is comparable to the size of the pristine material. Particle agglomeration is one of the main origins of capacity loss in TMF cathodes.<sup>10</sup> We attribute this behavior to the robust CEI derived from the IL electrolyte.<sup>27</sup> The negligible variation in cell impedance before and after cycling supports this observation (Figure S17). The surface of the cycled particle is partially covered in a grainy texture, which might originate from surface-trapped metallic iron. At larger magnifications, two types of morphology can be observed. In Figure 3D, the STEM image of an active material particle and its corresponding Fourier transform shown as inset display short-range ordering with an amorphous halo, respectively. For another particle (Figure S18), the absence of lattice fringes is observed. This morphology is fundamentally different from the single-crystalline pristine particles described above and indicates that the active material undergoes structural changes throughout extensive cycling. This is corroborated by *ex situ* XRD shown in Figure S19, where the cathode cycled 505 times did not display any diffraction peaks. EDX analysis of another cycled  $\text{FeF}_2$  particle shows a uniform distribution of iron, oxygen, and fluorine atoms in the particle.

To further investigate the bulk active material composition, X-ray absorption near-edge structure (XANES) spectroscopy was used to characterize a pristine cathode,



and the cycled cathodes (cycles 2 and 505) are shown in Figure 3E. A comparison of Fe K-edge spectra reveals that the white line intensity is significantly reduced in the cycled cathode, a change indicative of either a lower overall iron oxidation state in the cathode material or a less defined electronic structure. Since all three cathodes exhibit similar edge energies (7,126.2, 7,125.8, and 7,125.1 eV), a drastic change in oxidation state (e.g., continued formation of metallic iron) is unlikely. In view of the increasing disorder and reduced crystallinity detected by XRD, and the loss of defined FeF<sub>2</sub> particle morphology (Figure 3D), we suggest the decreased white line intensity to be rooted in a continuing amorphization of the active material. In addition, the cycled cathodes exhibit a pre-edge feature which is characteristic for Fe<sup>3+</sup>-oxygen species such as Fe<sub>2</sub>O<sub>3</sub> or Fe<sub>3</sub>O<sub>4</sub> but is not expected in FeF<sub>x</sub> compound.<sup>55,56</sup> This further validates the presence of an iron oxide phase in the bulk of the cycled active material.

Considering all of the above, we suggest the following aging mechanism of FeF<sub>2</sub> cathodes in the LiFSI Pyr<sub>1,3</sub>FSI electrolyte. From the first cycle on, FeF<sub>2</sub> exhibits an incomplete reconversion reaction with trapped metallic iron on the surface of the active material. Some of the metallic iron on the surface reacts over the course of several hundred cycles with oxygen-containing electrolyte decomposition products in the CEI, gradually forming Fe<sub>x</sub>O<sub>y</sub> during recharge. Lithium oxide, sulfonyl oxygen, and organic oxygen compounds were detected in the CEI (Figure S16) and were previously reported by our group.<sup>27</sup> As a result, excess charge capacity can be observed, which results in CE fluctuating between 95% and 99% (Figure 2D). Simultaneously, an additional redox plateau appears at low potentials. We estimate that after 500 cycles, approximately 20% of the total capacity originates from lithiation of the iron oxide species at low potentials, indicating that the oxide layer extends into the bulk of the active material.

Further, TEM, XRD, and X-ray absorption spectroscopy (XAS) analysis indicate a gradual amorphization of the active material. The evolving iron oxide phase does not share semi-coherent lattice interphases with the existing fluoride anion-host structure and thus results in a loss of long-range ordering and, ultimately, amorphization. Our results suggest that the cycled cathode exhibits faster reaction kinetics as a reduced voltage and improved energy efficiencies are observed (70.6% to 72.8% from the 2<sup>nd</sup> to 505<sup>th</sup> cycle). An earlier study comparing crystalline and amorphous FeF<sub>2</sub> using the galvanostatic intermittent titration technique determined faster reaction kinetics in the amorphous material.<sup>49</sup>

[FSI]<sup>−</sup> is the only oxygen-containing active component in the cell. Since the iron oxide phase gradually forms throughout cycling, [FSI]<sup>−</sup> anions are expected to be consumed beyond the initial CEI and solid electrolyte interphase (SEI) formation. Due to the presence of excess electrolyte, cell performance in this work has not been significantly affected. To quantify the amount of [FSI]<sup>−</sup> consumption, the LiFSI concentration in the electrolyte was measured (Figure S20).

During the course of 500 cycles, we observed a reduction in LiFSI concentration, decreasing from an initial value of 0.98 mol L<sup>−1</sup> to 0.94 mol L<sup>−1</sup>. This decrease corresponds to an [FSI]<sup>−</sup> consumption rate of 11 μmol g<sup>−1</sup> per cycle. It is important to acknowledge that the lithium metal anode is also anticipated to play a role in the depletion of [FSI]<sup>−</sup>, and there is also the likelihood of [Pyr<sub>1,3</sub>]<sup>+</sup> being consumed, which adds complexity to the calculation of the LiFSI concentration decline. As a result, a more comprehensive analysis of electrolyte consumption is essential for accurately determining the rate of [FSI]<sup>−</sup> consumption.

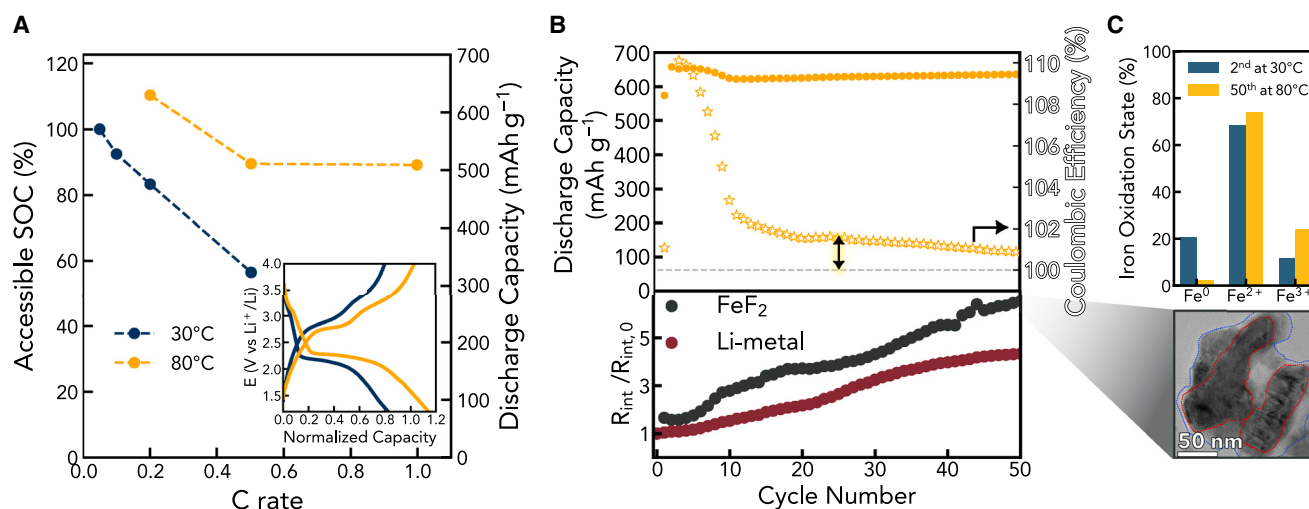


**Figure 4. Investigating the electrochemical behavior at elevated temperatures**

(A) Accessible state-of-charge as a function of cycling rate at different temperatures. The inset shows the corresponding normalized GCPL at 30°C and 80°C.

(B) Discharge capacity of three-electrode cells cycling FeF<sub>2</sub>-IL at 80°C at a C/5 rate. Below are the corresponding cathode and anode interphase impedances as a function of cycle number determined by electrochemical impedance spectroscopy.

(C) Iron oxidation state determined by XPS of the cathode cycled 50 times at 80°C and twice at 30°C. Below is a TEM image of the particles found in the cathode cycled 50 times at 80°C.

### Investigating the electrochemical behavior at elevated temperatures

Electric flight applications require high power loads during take-off and landing.<sup>2,3,57</sup> At larger discharge currents, a large overpotential limits the accessible capacity of FeF<sub>2</sub> cathodes, particularly at a high active material content. The high thermal stability of TMF cathodes and IL electrolytes enables cell operation at elevated temperatures. Higher thermal energy increases ion transport and reaction kinetics, improving rate capability.<sup>24,27,28,58,59</sup> Battery packs in electric aircraft contain active cooling to control the operating temperature. By carefully managing the active cooling system, a controlled battery heat-up during flight sections that require critical power loads could enhance the power output capabilities of FeF<sub>2</sub> cathodes. Therefore, we investigated the electrochemical performance of FeF<sub>2</sub>-IL cells at elevated temperatures.

The normalized GCPLs of FeF<sub>2</sub> cells (third cycle) at 30°C and 80°C are plotted in Figure 4A (inset). With increasing temperature, the overpotential decreases and, thus, the corresponding energy efficiencies increase from 71.3% to 77.0%. Figure 4A shows the accessible SOC and discharge capacity for different cycling rates. Around 90% of SOC can be accessed at 1 C at 80°C. A 1-C discharging speed of FeF<sub>2</sub> cathodes corresponds to approximately 1.3 kW kg<sup>-1</sup>, which satisfies power requirements during take-off and landing in some electric aircraft designs.<sup>57</sup>

To test whether the same cycling stability can be maintained at elevated temperatures, three-electrode cells were prepared. Using a lithium metal reference electrode enables the deconvolution of interphase impedances from the CEI and SEI, respectively, and thus can provide insights into the electrode interphase stability under galvanostatic conditions. Figure 4B shows the discharge capacity, CE, and both cathode and anode interphase impedances as a function of cycle number at 80°C. The corresponding GCPL for the working and counter electrode can be found in Figure S21.

The cell cycled at 80°C shows an increase of discharge capacity in the first ten cycles beyond the theoretical capacity of FeF<sub>2</sub> (571 mA h g<sup>-1</sup>) before it stabilizes at about 630 mA h g<sup>-1</sup> for over 50 cycles. Concurrently, the CE increases to around 110% before stabilizing at around 100.8%. A comparison with a cell cycled at 30°C shows that both discharge capacity and CE are increased at elevated temperatures (Figure S22). The CE of more than 100% indicates that continuous electrolyte consumption contributes to the faradic current. Accordingly, the normalized cathode and anode interphase impedances steadily increase at 80°C in contrast to the cell cycled at 30°C, which displays constant interphase impedance (Figures 4B, S17, and S22). An increase in temperatures accelerates and exacerbates the parasitic reaction, resulting in a higher CE, SEI, and CEI growth.

TEM imaging of cycled particles showed the presence of a 10-nm-thick amorphous layer covering the cycled FeF<sub>2</sub> particles, as shown in Figure 4C. Even at elevated temperatures the particles did not fuse, maintaining a primary particle size within the diffusion length of lithium ions and consequently enabling full capacity retention.

When comparing the iron oxidation state composition determined by XPS (Figures 4C and S23) of charged particles at 30°C and 80°C, it becomes evident that no metallic iron is present in the cell operated at 80°C. This observation aligns well with the increased accessible capacity compared to operation cycling at 30°C. As thermal energy increases, the diffusion length of Li<sup>+</sup> cations in FeF<sub>2</sub> increases, allowing the conversion of the previously inaccessible inner particle core.

Moreover, the inset in Figure 4A highlights an increased capacity contribution from the potential plateau at 3.1 V vs. Li<sup>+</sup>/Li at 80°C, attributed to a FeF<sub>3</sub> + e<sup>-</sup> → FeF<sub>2</sub> redox process (theoretical specific capacity of 237 mA h g<sup>-1</sup>).<sup>27,28,31</sup> Postmortem XPS analysis (Figure 4C) also confirms a higher Fe<sup>3+</sup> content in the charged cathode compared to a cell cycled at 30°C. This additional capacity accounts for the specific capacity exceeding the theoretical value for FeF<sub>2</sub>. The additional fluoride necessary for the formation of FeF<sub>3</sub> might stem from the decomposition products in the CEI. Further experiments are needed to verify this hypothesis.

Our results demonstrate that the FeF<sub>2</sub>-IL cells can be cycled reversibly at up to 120°C (see Figure S24 for capacity retention as a function of cycle number). With increasing temperature, more Fe<sup>3+</sup> is accessed, the voltage hysteresis is reduced, and rate capability is improved, increasing overall the energy and power density of the cells.

The upper temperature limit of the proposed cell chemistry was studied using a custom-made *in situ* thermal analysis cell setup as described in more detail in Figures S25–S27). Our results indicate the full-cell configuration is stable up to the melting point of lithium of 181°C, providing further versatility for high-temperature applications and improved safety features over conventional cell chemistries.

## Conclusion

In this study, we provide a systematic investigation of FeF<sub>2</sub> cathodes and identify the crucial role played by particle size and composite preparation technique in the electrochemical performance. We developed a CD composite preparation technique with improved electronic conductivity that enables full capacity retention over 500 cycles and unprecedented cell performance for active material contents up to 85%. To test whether the cycling performance could be reproduced in larger electrodes, a 42 mA h (32.64 cm<sup>2</sup>) pouch cell with a 30-μm-thin lithium metal anode was prepared. Figure 5A shows the discharge capacity as a function of cycle number

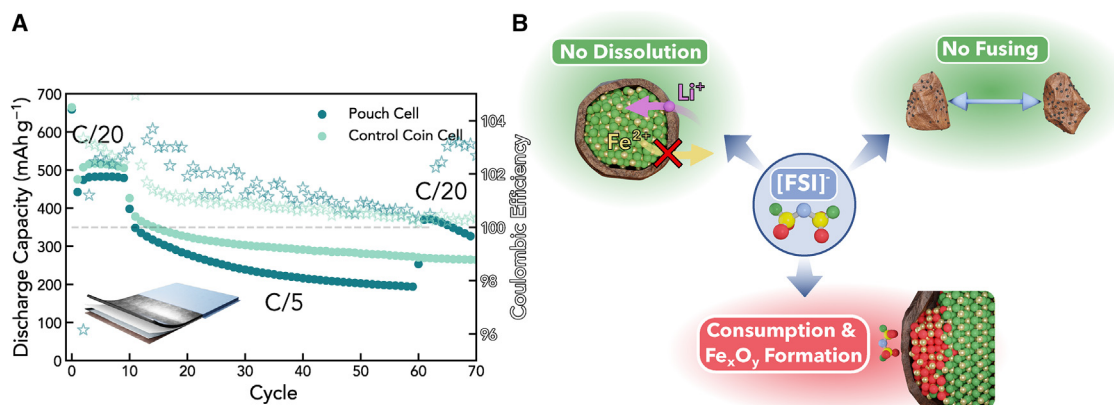


**Figure 5. Role of  $[\text{FSI}]^-$**

(A) Discharge capacity (dots) and Coulombic efficiency (stars) of a pouch cell and a control coin cell using a  $\text{FeF}_2$  cathode in a  $\text{LiFSI Pyr}_{1,3}\text{FSI}$  electrolyte and a  $30\text{-}\mu\text{m}$  lithium metal anode. The pouch cell has a capacity of  $42\text{ mA h}$  and a cathode surface area of  $32.64\text{ cm}^2$ . Excess amounts of electrolyte were used (approximately  $150\text{ mL g}^{-1}$ ).

(B) Schematic overview of the role of bis(fluorosulfonyl)imide anions on the cycling performance of  $\text{FeF}_2$  cathodes.  $[\text{FSI}]^-$  enables the formation of a CEI, which prevents active material dissolution and particle fusing. However, over extensive cycling  $[\text{FSI}]^-$  decomposition products are consumed, and a redox-active  $\text{Fe}_x\text{O}_y$  phase is formed.

compared to a control coin cell. The pouch cell performs similarly to the coin cell and can reversibly access over  $480\text{ mA h g}^{-1}$  at slow cycling rates while showing small capacity fading at a higher rate. Although the high capacity retention of  $\text{FeF}_2$  cathodes can be reproduced in a pouch-cell format, excess amounts of electrolyte were used to amend the following shortcomings of our current cell configuration. All cells prepared in this study comprise a glass fiber separator, due to the superior wetting properties of the IL electrolyte. In addition, the cathodes exhibit a porosity of around 66%. Considering the high viscosity of the IL electrolyte (approximately  $40\text{ cP}$ ), a reduction of porosity could lead to insufficient wetting of the active material, thus affecting the accessible capacity. As a result of the highly porous separator and cathode, excess electrolyte per cathode material (around  $150\text{ mL g}^{-1}$ ) was used in the coin- and pouch-cell formats, which significantly reduces their practical energy density. More importantly, as shown in this study,  $[\text{FSI}]^-$  is an integral component in forming a passivating CEI, which prevents particle fusing and active material dissolution and thus enables high cycling reversibility (Figure 5B). However, the gradual formation of a redox-active oxide phase is correlated with  $[\text{FSI}]^-$  consumption. With a rough consumption rate estimate of  $11\text{ }\mu\text{mol g}^{-1}$  per cycle, impractical amounts of  $[\text{FSI}]^-$  are required to keep the  $\text{LiFSI}$  concentration close to 1 at higher active material loadings. Consequently, to enable cell upscaling with competitive energy densities (see Figure S28 and Table S1 for energy density calculations), electrolyte optimization is required to stabilize the CEI and keep  $[\text{FSI}]^-$  consumption limited to the initial formation cycle.

The development of an appropriate electrolyte formulation would enable battery chemistry capable of advancing the electrification of the aviation industry.

## EXPERIMENTAL PROCEDURES

### Resource availability

#### Lead contact

Further information and requests for resources and reagents should be directed to and will be fulfilled by the lead contact, Mauro Pasta ([mauro.pasta@materials.ox.ac.uk](mailto:mauro.pasta@materials.ox.ac.uk)).

#### Materials availability

This study did not generate new unique reagents.

#### Data and code availability

All data reported in this paper will be shared by the [lead contact](#) upon request.

### SUPPLEMENTAL INFORMATION

Supplemental information can be found online at <https://doi.org/10.1016/j.xcrp.2024.101787>.

### ACKNOWLEDGMENTS

This work was supported by funding from the Engineering and Physical Sciences Research Council (grant number EP/R511742/1), the Henry Royce Institute for capital equipment (through UK Engineering and Physical Science Research Council grant EP/R010145/1), and the Army Research Office (ARO) (grant number W911NF-20-1-0210). The views and conclusions contained in this document are those of the authors and should not be interpreted as representing the official policies, either expressed or implied, of ARO or the US Government. The US Government is authorized to reproduce and distribute reprints for Government purposes notwithstanding any copyright notation herein. The authors would like to thank J. Gibson and P. Cong for their support with XAS measurements, B. Jagger and Y. Liang for their support with XPS measurements, L. Dai for his support with TEM measurements, and M. Forghani for her support with pouch-cell assembly.

### AUTHOR CONTRIBUTIONS

Conceptualization, L.F.O. and A.W.X.; data curation, L.F.O.; formal analysis, L.F.O. and J.I.; funding acquisition, L.F.O., M. Sanghadasan, and M.P.; investigation, L.F.O. and G.M.; methodology, L.F.O. and M.P.; validation, L.F.O.; visualization, L.F.O.; writing – original draft, L.F.O.; writing – review and editing, L.F.O., A.W.X., M. Scharf, and M.P.; project administration, M.P.; supervision, M.P.

### DECLARATION OF INTERESTS

The authors declare no competing interests.

Received: November 30, 2023

Revised: December 15, 2023

Accepted: January 5, 2024

Published: January 29, 2024

### REFERENCES

1. IEA (2020). Global EV Outlook 2020 – Analysis (IEA).
2. Viswanathan, V., Epstein, A.H., Chiang, Y.M., Takeuchi, E., Bradley, M., Langford, J., and Winter, M. (2022). The challenges and opportunities of battery-powered flight. *Nature* 601, 519–525.
3. Sripad, S., and Viswanathan, V. (2021). The promise of energy efficient battery-powered urban aircraft. *Proc. Natl. Acad. Sci. USA* 118, e2111164118.
4. Schäfer, A.W., Barrett, S.R., Doyme, K., Dray, L.M., Gnad, A.R., Self, R., O'Sullivan, A., Synodinos, A.P., and Torija, A.J. (2019). Technological, economic and environmental prospects of all-electric aircraft. *Nature Energy* 4, 160–166.
5. Lin, X., Salari, M., Arava, L.M.R., Ajayan, P.M., and Grinstaff, M.W. (2016). High temperature electrical energy storage: Advances, challenges, and frontiers. *Chem. Soc. Rev.* 45, 5848–5887.
6. Bills, A., Sripad, S., Fredericks, W.L., Singh, M., and Viswanathan, V. (2020). Performance Metrics Required of Next-Generation Batteries to Electrify Commercial Aircraft. *ACS Energy Lett.* 5, 663–668.
7. Bills, A., Sripad, S., Fredericks, L., Guttenberg, M., Charles, D., Frank, E., and Viswanathan, V. (2023). A battery dataset for electric vertical takeoff and landing aircraft. *Sci. Data* 10, 344–347.
8. Fredericks, W.L., Sripad, S., Bower, G.C., and Viswanathan, V. (2018). Performance Metrics Required of Next-Generation Batteries to Electrify Vertical Takeoff and Landing (VTOL) Aircraft. *ACS Energy Lett.* 3, 2989–2994.
9. Wang, L., Luo, Z., Xu, H., Piao, N., Chen, Z., Tian, G., and He, X. (2019). Anion effects on the solvation structure and properties of imide lithium salt-based electrolytes. *RSC Adv.* 9, 41837–41846.
10. Olbrich, L.F., Xiao, A.W., and Pasta, M. (2021). Conversion-type fluoride cathodes: Current



- state of the art. *Curr. Opin. Electrochem.* **30**, 100779.
11. Sun, L., Li, Y., and Feng, W. (2023). Metal Fluoride Cathode Materials for Lithium Rechargeable Batteries: Focus on Iron Fluorides. *Small Methods* **7**, e2201152.
12. Nikitin, M.I., Chilingarov, N.S., and Alikhanyan, A.S. (2021). Thermal Stability of Mixed Fluorides of 3d Elements. *Russ. J. Inorg. Chem.* **66**, 89–95.
13. Lin, Y., Hu, Q., Zhu, L., and Meng, Y. (2020). Structure and stability of iron fluoride at high pressure–temperature and implication for a new reservoir of fluorine in the deep earth. *Minerals* **10**, 783–787.
14. Wu, F., Maier, J., and Yu, Y. (2020). Guidelines and trends for next-generation rechargeable lithium and lithium-ion batteries. *Chem. Soc. Rev.* **49**, 1569–1614.
15. Wu, F., and Yushin, G. (2017). Conversion cathodes for rechargeable lithium and lithium-ion batteries. *Energy Environ. Sci.* **10**, 435–459.
16. Badway, F., Cosandey, F., Pereira, N., and Amatucci, G.G. (2003). Carbon Metal Fluoride Nanocomposites. *J. Electrochem. Soc.* **150**, A1318.
17. Doe, R.E., Persson, K.A., Meng, Y.S., and Ceder, G. (2008). First-principles investigation of the Li-Fe-F phase diagram and equilibrium and nonequilibrium conversion reactions of iron fluorides with lithium. *Chem. Mater.* **20**, 5274–5283.
18. Wang, F., Robert, R., Chernova, N.A., Pereira, N., Omenya, F., Badway, F., Hua, X., Ruotolo, M., Zhang, R., Wu, L., et al. (2011). Conversion reaction mechanisms in lithium ion batteries: Study of the binary metal fluoride electrodes. *J. Am. Chem. Soc.* **133**, 18828–18836.
19. Wang, F., Yu, H.C., Chen, M.H., Wu, L., Pereira, N., Thornton, K., Van Der Ven, A., Zhu, Y., Amatucci, G.G., and Graetz, J. (2012). Tracking lithium transport and electrochemical reactions in nanoparticles. *Nat. Commun.* **3**, 1201–1208.
20. Li, C., Gu, L., and Maier, J. (2012). Enhancement of the Li conductivity in LiF by introducing glass/crystal interfaces. *Adv. Funct. Mater.* **22**, 1145–1149.
21. Ma, Y., and Garofalini, S.H. (2012). Atomistic insights into the conversion reaction in iron fluoride: A dynamically adaptive force field approach. *J. Am. Chem. Soc.* **134**, 8205–8211.
22. Garofalini, S.H. (2014). Interplay between the ionic and electronic transport and its effects on the reaction pattern during the electrochemical conversion in an FeF<sub>2</sub> nanoparticle. *Phys. Chem. Chem. Phys.* **16**, 11690–11697.
23. Li, L., Chen-Wiegar, Y.C.K., Wang, J., Gao, P., Ding, Q., Yu, Y.S., Wang, F., Cabana, J., Wang, J., and Jin, S. (2015). Visualization of electrochemically driven solid-state phase transformations using operando hard X-ray spectro-imaging. *Nat. Commun.* **6**, 6883.
24. Li, L., Jacobs, R., Gao, P., Gan, L., Wang, F., Morgan, D., and Jin, S. (2016). Origins of Large Voltage Hysteresis in High-Energy-Density Metal Fluoride Lithium-Ion Battery Conversion Electrodes. *J. Am. Chem. Soc.* **138**, 2838–2848.
25. Li, C., Chen, K., Zhou, X., and Maier, J. (2018). Electrochemically driven conversion reaction in fluoride electrodes for energy storage devices. *npj Comput. Mater.* **4**, 22.
26. Karki, K., Wu, L., Ma, Y., Armstrong, M.J., Holmes, J.D., Garofalini, S.H., Zhu, Y., Stach, E.A., and Wang, F. (2018). Revisiting Conversion Reaction Mechanisms in Lithium Batteries: Lithiation-Driven Topotactic Transformation in FeF<sub>2</sub>. *J. Am. Chem. Soc.* **140**, 17915–17922.
27. Xiao, A.W., Lee, H.J., Capone, I., Robertson, A., Wi, T.U., Fawdon, J., Wheeler, S., Lee, H.W., Grobert, N., and Pasta, M. (2020). Understanding the conversion mechanism and performance of monodisperse FeF<sub>2</sub> nanocrystal cathodes. *Nat. Mater.* **19**, 644–654.
28. Hua, X., Eggeman, A.S., Castillo-Martínez, E., Robert, R., Geddes, H.S., Lu, Z., Pickard, C.J., Meng, W., Wiaderek, K.M., Pereira, N., et al. (2021). Revisiting metal fluorides as lithium-ion battery cathodes. *Nat. Mater.* **20**, 841–850.
29. Song, H., Cui, H., and Wang, C. (2015). Extremely high-rate capacity and stable cycling of a highly ordered nanostructured carbon-FeF<sub>2</sub> battery cathode. *J. Mater. Chem. A Mater.* **3**, 22377–22384.
30. Guntlin, C.P., Zünd, T., Kravchyk, K.V., Wörle, M., Bodnarchuk, M.I., and Kovalenko, M.V. (2017). Nanocrystalline FeF<sub>3</sub> and MF<sub>2</sub> (M = Fe, Co, and Mn) from metal triuoroacetates and their Li(Na)-ion storage properties. *J. Mater. Chem. A Mater.* **5**, 7383–7393.
31. Fu, W., Zhao, E., Sun, Z., Ren, X., Magasinski, A., and Yushin, G. (2018). Iron Fluoride/Carbon Nanocomposite Nanofibers as Free-Standing Cathodes for High-Energy Lithium Batteries. *Adv. Funct. Mater.* **28**, 1–8.
32. Huang, Q., Lee, Y.Y., and Gurkan, B. (2019). Pyrrolidinium Ionic Liquid Electrolyte with Bis(tri uoromethylsulfonyl)imide and Bis(fluorosulfonyl)imide Anions: Lithium Solvation and Mobility, and Performance in Lithium Metal-Lithium Iron Phosphate Batteries. *Ind. Eng. Chem. Res.* **58**, 22587–22597.
33. Zhai, J., Lei, Z., and Sun, K. (2019). 3D Starfish-Like FeOF on Graphene Sheets: Engineered Synthesis and Lithium Storage Performance. *Chemistry (Basel)* **25**, 7733–7739.
34. Wu, W., Wang, S., Wu, W., Chen, K., Hong, S., and Lai, Y. (2019). A critical review of battery thermal performance and liquid based battery thermal management. *Energy Convers. Manag.* **182**, 262–281.
35. Wu, F., Srot, V., Chen, S., Zhang, M., Van Aken, P.A., Wang, Y., Maier, J., and Yu, Y. (2021). Metal-Organic Framework-Derived Nanoconfinement of CoF<sub>2</sub> and Mixed-Conducting Wiring for High-Performance Metal Fluoride-Lithium Battery. *ACS Nano* **15**, 1509–1518.
36. Guan, T., Zhao, L., Zhou, Y., Qiu, X., Wu, J., Wu, G., and Bao, N. (2023). Hetero-Packing Nanostructures of Iron (III) Fluoride Nanocomposite Cathode for High-Rate and Long-Life Rechargeable Lithium-Ion Batteries. *Adv. Energy Mater.* **13**, 1–9.
37. Zhou, J., Zhang, D., Zhang, X., Song, H., and Chen, X. (2014). Carbon-nanotube-encapsulated FeF<sub>2</sub> nanorods for high-performance lithium-ion cathode materials. *ACS Appl. Mater. Interfaces* **6**, 21223–21229.
38. Hu, J., Zhang, Y., Cao, D., and Li, C. (2016). Dehydrating bronze ironfluoride as a high capacity conversion cathode for lithium batteries. *J. Mater. Chem. A Mater.* **4**, 16166–16174.
39. Tan, J., Liu, L., Hu, H., Yang, Z., Guo, H., Wei, Q., Yi, X., Yan, Z., Zhou, Q., Huang, Z., et al. (2014). Iron uoride with excellent cycle performance synthesized by solvothermal method as cathodes for lithium ion batteries. *J. Power Sources* **251**, 75–84.
40. Capone, I., Hurlbutt, K., Naylor, A.J., Xiao, A.W., and Pasta, M. (2019). Effect of the Particle-Size Distribution on the Electrochemical Performance of a Red Phosphorus-Carbon Composite Anode for Sodium-Ion Batteries. *Energy Fuels* **33**, 4651–4658.
41. Zhou, Y., Xu, L., Liu, M., Qi, Z., Wang, W., Zhu, J., Chen, S., Yu, K., Su, Y., Ding, B., et al. (2022). Viscous Solvent-Assisted Planetary Ball Milling for the Scalable Production of Large Ultrathin Two-Dimensional Materials. *ACS Nano* **16**, 10179–10187.
42. Pasta, M., Albert, W., and XIAO. (2019). Ionic Liquids in Lithium Ion Batteries.
43. Shkrob, I.A., Marin, T.W., Zhu, Y., and Abraham, D.P. (2014). Why bis(fluorosulfonyl)imide is a “magic anion” for electrochemistry. *J. Phys. Chem. C* **118**, 19661–19671.
44. Huang, Q., Turcheniuk, K., Ren, X., Magasinski, A., Gordon, D., Bensalah, N., and Yushin, G. (2019). Insights into the Effects of Electrolyte Composition on the Performance and Stability of FeF<sub>2</sub> Conversion-Type Cathodes. *Adv. Energy Mater.* **9**, 1–11.
45. Ko, J.K., Wiaderek, K.M., Pereira, N., Kinnibrugh, T.L., Kim, J.R., Chupas, P.J., Chapman, K.W., and Amatucci, G.G. (2014). Transport, phase reactions, and hysteresis of ironfluoride and oxyfluoride conversion electrode materials for lithium batteries. *ACS Appl. Mater. Interfaces* **6**, 10858–10869.
46. Li, C., Gu, L., Tong, J., and Maier, J. (2011). Carbon nanotube wiring of electrodes for high-rate lithium batteries using an imidazolium-based ionic liquid precursor as dispersant and binder: A case study on ironfluoride nanoparticles. *ACS Nano* **5**, 2930–2938.
47. Myung, S.T., Sakurada, S., Yashiro, H., and Sun, Y.K. (2013). Iron trifluoride synthesized via evaporation method and its application to rechargeable lithium batteries. *J. Power Sources* **223**, 1–8.
48. Liu, L., Guo, H., Zhou, M., Wei, Q., Yang, Z., Shu, H., Yang, X., Tan, J., Yan, Z., and Wang, X. (2013). A comparison among FeF<sub>3</sub>·3H<sub>2</sub>O, FeF<sub>3</sub>·0.33H<sub>2</sub>O and FeF<sub>3</sub> cathode materials for lithium ion batteries: Structural, electrochemical, and mechanism studies. *J. Power Sources* **238**, 501–515.
49. Shao, B., Tan, S., Huang, Y., Zhang, L., Shi, J., Yang, X.Q., Hu, E., and Han, F. (2022). Enabling Conversion-Type Iron Fluoride Cathode by Halide-Based Solid Electrolyte. *Adv. Funct. Mater.* **32**, 2206845.

50. Zhang, L., Wu, H.B., Madhavi, S., Hng, H.H., and Lou, X.W.D. (2012). Formation of Fe<sub>2</sub>O<sub>3</sub> microboxes with hierarchical shell structures from metal-organic frameworks and their lithium storage properties. *J. Am. Chem. Soc.* **134**, 17388–17391.
51. Zhang, L., Wu, H.B., and Lou, X.W.D. (2013). Metal-organic frameworks- derived general formation of hollow structures with high complexity. *J. Am. Chem. Soc.* **135**, 10664–10672.
52. Ito, S., Nakaoka, K., Kawamura, M., Ui, K., Fujimoto, K., and Koura, N. (2005). Lithium battery having a large capacity using Fe<sub>3</sub>O<sub>4</sub> as a cathode material. *J. Power Sources* **146**, 319–322.
53. Su, Y., Chen, J., Li, H., Sun, H., Yang, T., Liu, Q., Ichikawa, S., Zhang, X., Zhu, D., Zhao, J., et al. (2022). Enabling Long Cycle Life and High Rate Iron Difluoride Based Lithium Batteries by In Situ Cathode Surface Modification. *Adv. Sci.* **9**, e2201419.
54. Grosvenor, A.P., Kobe, B.A., Biesinger, M.C., and McIntyre, N.S. (2004). Investigation of multiplet splitting of Fe 2p XPS spectra and bonding in iron compounds. *Surf. Interface Anal.* **36**, 1564–1574.
55. Westre, T.E., Kennepohl, P., Dewitt, J.G., Hedman, B., Hodgson, K.O., Solomon, E.I., and V, S.U. (1997). A Multiplet Analysis of Fe K-Edge 1s f 3d Pre-Edge Features of Iron Complexes. *J. Am. Chem. Soc.* **7863**, 6297–6314.
56. Simon, H., Cibir, G., Freestone, I., and Schofield, E. (2021). Fe K-edge x-ray absorption spectroscopy of corrosion phases of archaeological iron: Results, limitations, and the need for complementary techniques. *J. Phys. Condens. Matter* **33**, 344002.
57. Moore, M. (2023). Whisper Aero Reveal Part 8: The Whisper Jet. Tech. rep. Whisper Aero.
58. Yu, H.C., Ling, C., Bhattacharya, J., Thomas, J.C., Thornton, K., and Van Der Ven, A. (2014). Designing the next generation high capacity battery electrodes. *Energy Environ. Sci.* **7**, 1760–1768.
59. Seo, J.K., Cho, H.M., Takahara, K., Chapman, K.W., Borkiewicz, O.J., Sina, M., and Shirley Meng, Y. (2017). Revisiting the conversion reaction voltage and the reversibility of the CuF<sub>2</sub> electrode in Li-ion batteries. *Nano Res.* **10**, 4232–4244.

**Cell Reports Physical Science, Volume 5**

**Supplemental information**

**Iron fluoride-lithium metal batteries  
in bis(fluorosulfonyl)imide-based ionic  
liquid electrolytes**

**Lorenz F. Olbrich, Albert W. Xiao, Maximilian Schart, Johannes Ihli, Guillaume Matthews, Mohan Sanghadasa, and Mauro Pasta**

## Supplemental Experimental Procedures

All chemical compounds and battery cell components are dried at 60°C under vacuum overnight before their usage and stored and handled under an argon atmosphere. Electrolytes are considered dry if a water content below 25 ppm is determined using Karl Fischer titration.

### Ball Milling

Ball milling was conducted using 7 grams of  $\text{FeF}_2$  (99.8%, Sigma-Aldrich), 7 milliliters of dry octadecene (Sigma-Aldrich), and 3 milliliters of dry oleic acid (Sigma-Aldrich) and 166 5-millimeter zirconia balls in a 45-milliliter jar (Fritsch) at different milling speeds. Each milling cycle lasted 5 minutes with a subsequent 7-minute rest. Samples were collected from the mill at various milling times and then washed three times using 2 milliliters of anhydrous ethanol and 10 milliliters of anhydrous hexane. All cathodes tested from the following section on were prepared from one milling batch which had a particle size range of D10-D90 140-330 nm, and a particle median of 226 nm. They were prepared by high energy milling at 700 rpm for 24 hours.

### Physical Characterization

For TEM measurements, the cathodes were loaded into a glass vial with anhydrous NMP and stirred for 24h under argon to disperse the active material and dissolve the binder. The dispersion was centrifuged and the supernatant was discarded. The resulting pellet was redispersed in fresh NMP, and dropcast on holey-carbon TEM grids (Agar) in a glovebox. All TEM samples were placed in a Schlenk tube under argon, dried under vacuum at 80°C overnight, and transported to the TEM in airtight vials under argon. Air exposure was limited to 30s during transfer to the TEM column. Bright-field TEM/HRTEM imaging was performed on a JEOL 3000F field emission gun transmission electron microscope operated at 300 kV and equipped with a Gatan Ultrascan charge-coupled device camera. SEM samples were prepared similar to TEM samples. Instead of drop casting onto a TEM grid, the dispersion was drop cast onto an aluminum stub. The cross-sections were realized by mounting electrodes on a Ti blade with Electrodag which were subsequently milled with an 8 kV Ar beam for 5 h using a Gatan PECS instrument. X-ray photoelectron spectroscopy (XPS) was performed with an ULVAC PHI Versaprobe III XPS system generating monochromatic AlK X-rays (1486.6 eV, 15 kV anode voltage, 25 W beam power) under ultrahigh vacuum (UHV) conditions ( $1\text{e-}7$  to  $1\text{e-}8$  Pascal). Samples were prepared in an argon-filled glovebox and were immediately transferred into the XPS chamber using a vacuum transfer vessel (ULVAC PHI GmbH) to avoid contamination and ambient exposure. A 500 micrometer times 500 micrometer area from each sample was analysed. Survey scans were acquired at pass energies of 224 eV, and a lower pass energy of 55 eV was used for core-level spectra. In-built electron and low-energy  $\text{Ar}^{+}$  sources were utilized for charge neutralization. Depth-profiling was achieved with consecutive XPS analysis and  $\text{Ar}^{+}$  sputtering (4 keV, 3 millimeter times 3 millimeter) for a total of 60 min. Acquired spectra were fitted with Voigt lineshapes, after the application of a Shirley background, using CasaXPS software. Data processing was conducted using CasaXPS software. Fe-K-edge XANES measurements were performed using a lab-source X-ray Absorption Spectrometer (XAS) from easyXAFS in transmission mode. Powdered samples, extracted from the respective cathode layers and synthesis batch, were diluted with cellulose and pressed into pellets. For the calibration of the incident beam energy, a pristine, standard  $\text{FeF}_2$  cathode was measured before the measurement. Reference spectra of  $\text{FeF}_2$ ,  $\text{FeF}_3$ ,  $\text{Fe}_3\text{O}_4$ ,  $\text{Fe}_2\text{O}_3$ ,  $\text{FeO}$ , and  $\text{Fe}$  were acquired. Spectra preprocessing, i.e., energy calibration, background subtraction, and edge-step normalization and XANES data analysis, i.e., edge energy determination, and compositional linear combination fitting were performed in Athena.

## Cell fabrication

All electrodes were fabricated using a conventional tape-casting method. The as-synthesized active material was dispersed in anhydrous hexane and mixed with Super-P carbon (TIMCAL) in different ways as described in the following section. The composite was dried under vacuum and hand-ground with additional Super-P before mixing with PVDF and NMP. The resulting slurry (70:20:10, FeF<sub>2</sub>: carbon black, 99+% Alfa Aesar:poly(vinylidene fluoride) Sigma Aldrich) was cast via doctor blade on aluminum foil dried in a fume hood for 24 hours and under vacuum for another 24 hours. Circular electrodes were punched with a diameter of 1 centimeter. All electrodes tested contained between 1.0 milligram per square centimeter and 2.0 milligrams per square centimeter active material. Ionic liquids were purchased from Solvionic (Pyr<sub>1,3</sub>FSI 99.5%) and dried under vacuum at 70°C. Electrolytes were prepared by solving 1 millimol of the respective salt (LiFSI from TCI >98%) per gram of IL. All cells were assembled in an argon-filled glovebox using glass fiber separators (Whatman, GF/D), metallic lithium foil (Sigma, 99.9%) as the counter/reference electrodes, and 150 microliters of electrolyte. For batteries operating at 30°C, regular 2032 coin cell components with a polypropylene gasket were used (MTI Corporation). For higher temperatures, 2032 coin cell components with a temperature-resistant perfluoroalkoxy alkane gasket were used to prevent cell leakage (Hohsen Corporation). Cell cases in contact with the working electrode are aluminum coated (CVD) from both suppliers to prevent corrosion at high potentials. Cells were cycled between 4.0 volts and 1.2 volts in an oven using either a Biologic BCS-805 battery cycler or a Biologic VMP3 potentiostat. Three-electrode cells were prepared using commercial ECC-Ref cells from EL-CELL and lithium reference electrodes.

## 4-probe measurement

By passing a current through the two outer probes and measuring the voltage drop of the two inner ones, it is possible to eliminate the contact resistances. Since the probe spacing is much smaller than the casting surface area, the geometric factor for an infinitely large, thin slice can be used to calculate the sheet resistance:

$$\rho_{\text{cond}} = (\pi / \ln(2)) \cdot t \cdot (V / I)$$

Here,  $t$  is the thickness of the casting (15 micrometers) while  $I$  and  $V$  correspond to the applied current and the measured voltage difference respectively.



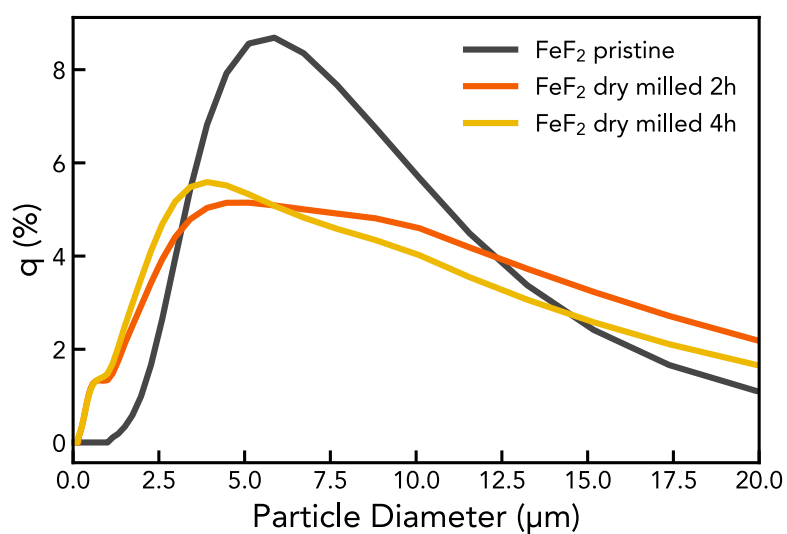


**Figure S1. Dry Milling** Particle size distribution determined by DLS (volume fraction) for FeF<sub>2</sub> particles during dry milling at 500 rpm.

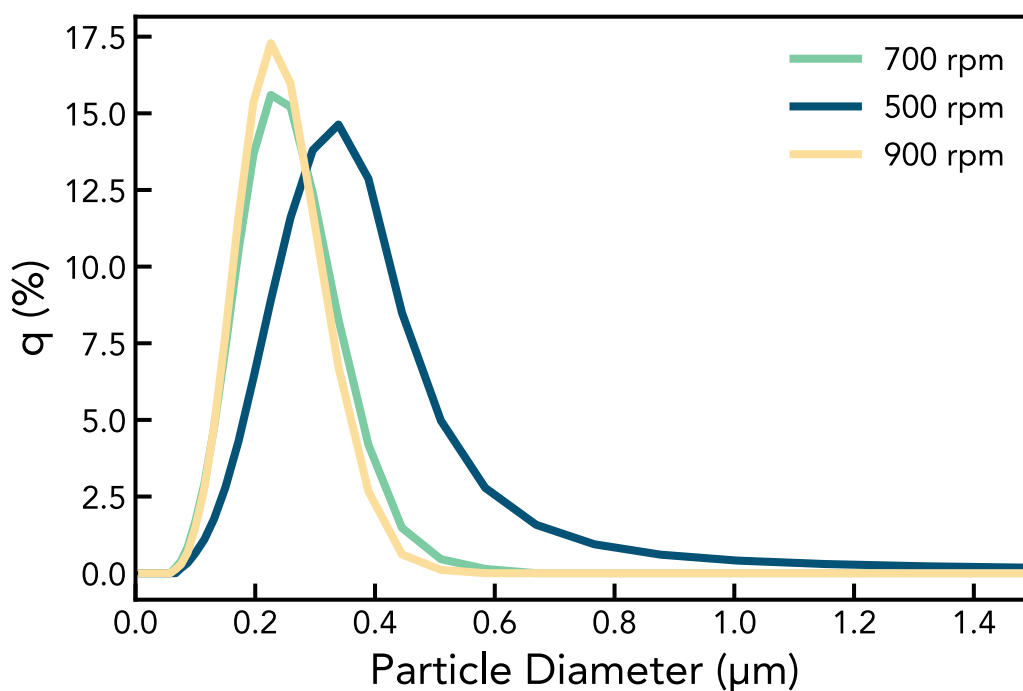


**Figure S2. Wet Milling** Particle size distribution determined by DLS (volume fraction) for FeF<sub>2</sub> particles ball milled at different rotation speeds.

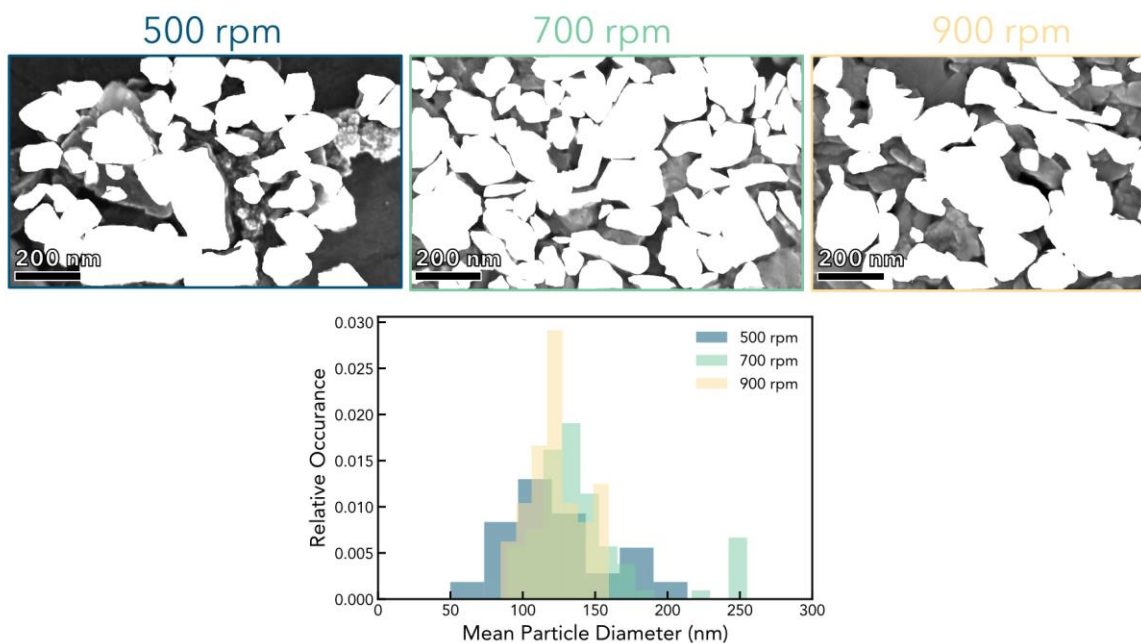


**Figure S3. Particle Size Distribution** Statistical analysis of particle size from SEM images. Threshold was selected manually across images. Below is shown the image derives particle size distribution. In each image, at 45 to 85 particles were counted and the size distribution was normalized accordingly.

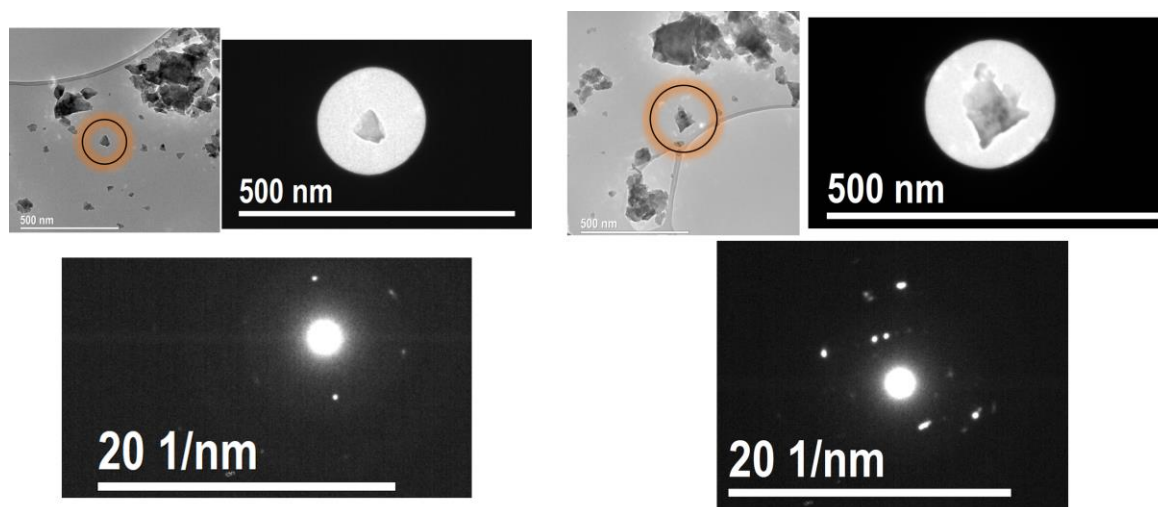


**Figure S4. Electron Diffraction** Post-milling electron diffraction of ball milled  $\text{FeF}_2$ . Two particles are shown exemplarily. Both of which exhibit single crystallinity.

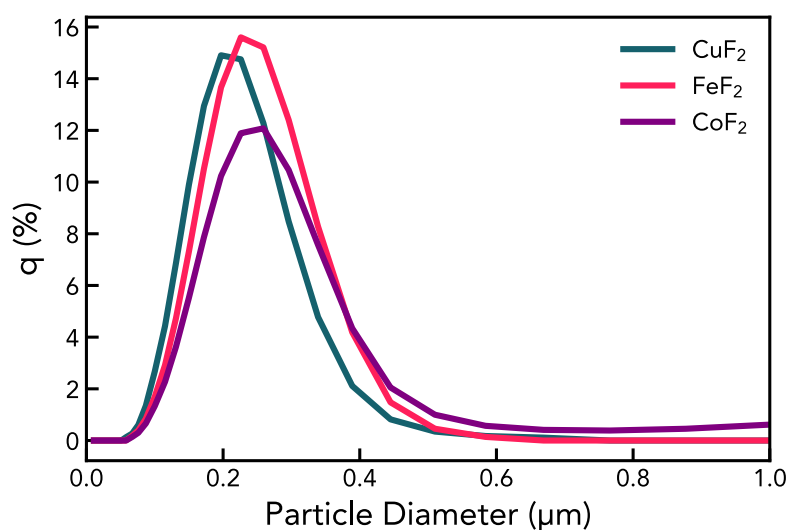


**Figure S5. Particle Size of other Transition Metal Fluorides** Particle size distribution determined by DLS (volume fraction) for different transition metal fluoride cathodes. The commercial powder was milled for 5 min on, 7min off, in total 12h at 700rpm.

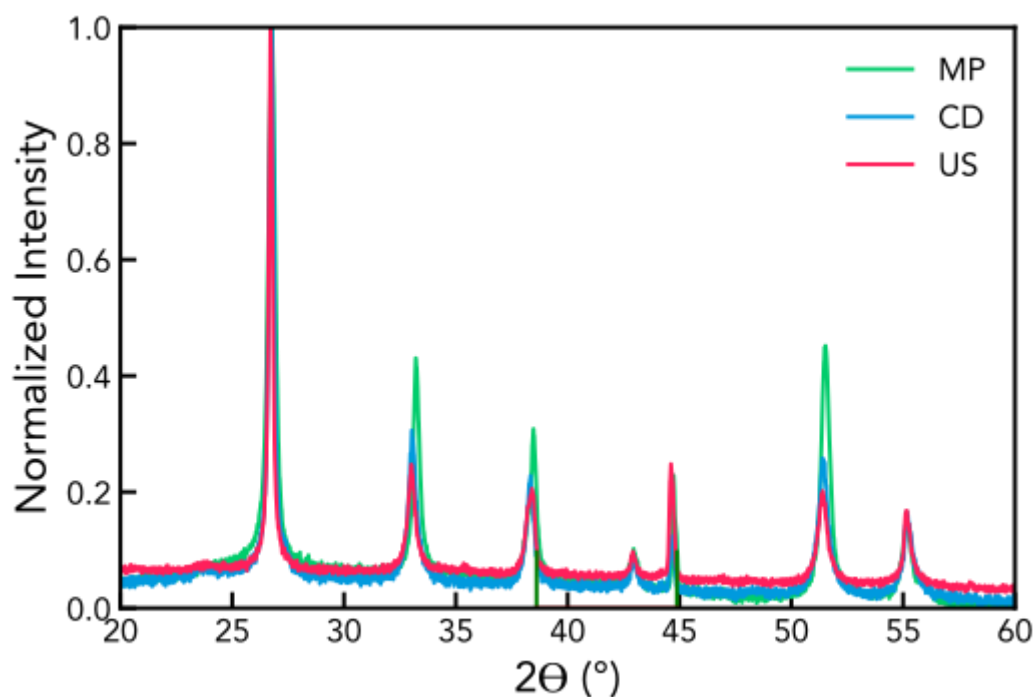


**Figure S6. XRD of Cathode Composites** Powder XRD of cathodes from three different composites. Patterns were collected using a monochromated Cu K $\alpha$  X-ray source from 20° to 60° 2 $\theta$ , at a scan rate of 1deg/min. The green lines indicate the diffraction peaks of the underlying aluminium current collector.

Mortar & Pestle (MP) Co-dispersion (CD) Ultra stirred (US)

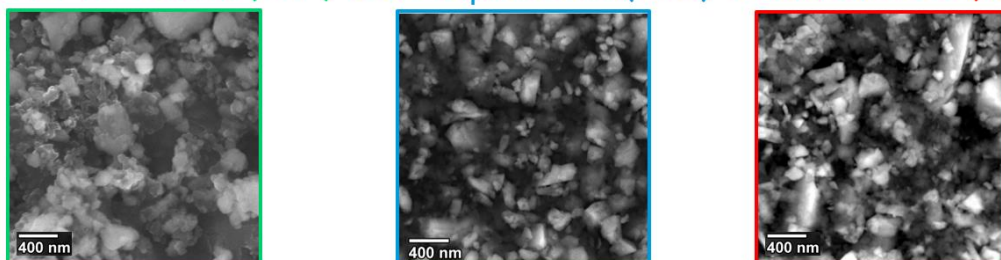


**Figure S7. Top-View SEM** Top-view SEM images of the three different  $\text{FeF}_2$  composites discussed in the main text.

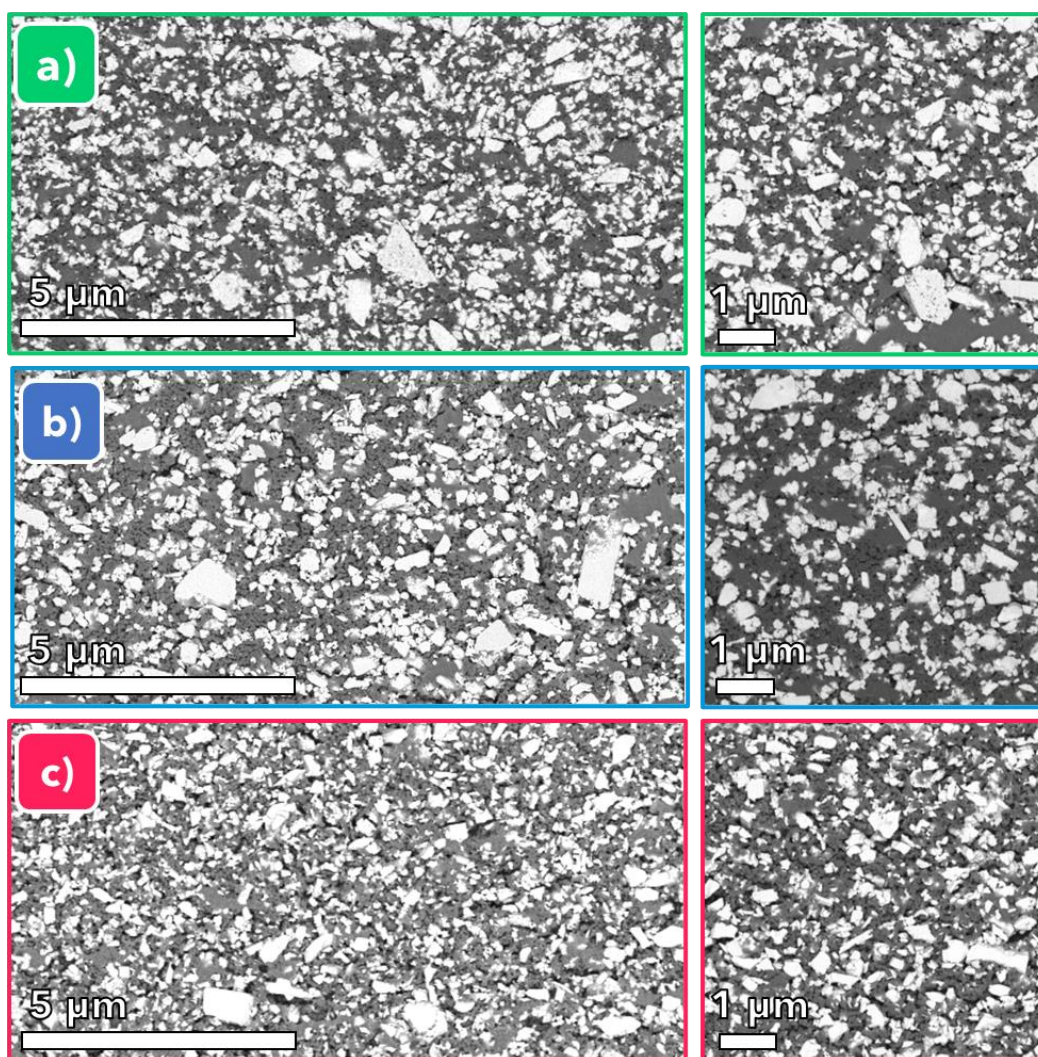


**Figure S8. Cross Section SEM** Cross-section SEM images prepared with broad beam argon milling tool (Gatan Precision Etching Coating System or PECS using a Ti-blade with electrodag; 8kV Ar beam for 5h) of the three different  $\text{FeF}_2$  composites, a) Mortar & Pestle, b) Co-dispersion, and c) ultra-stirred. The images on the right correspond to the same area of the EDX images illustrated in Figure 2b in the main text.

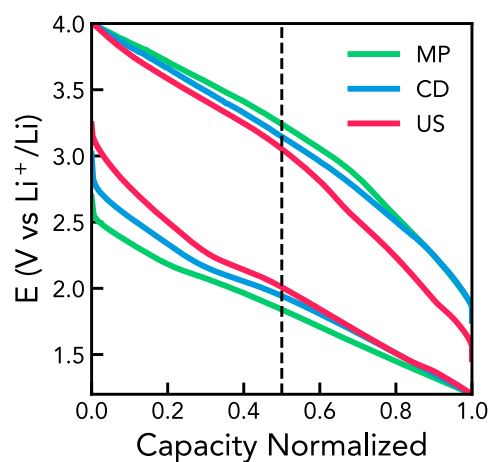


**Figure S9. Voltage Hysteresis** GCPL of three different composites, mortar and pestle (MP), co-dispersion (CD), and ultra-stirring (US), at the 50th cycle in a 1M LiFSI Pyr<sub>1,3</sub>FSI electrolyte at 30°C at a C/5 cycling rate.

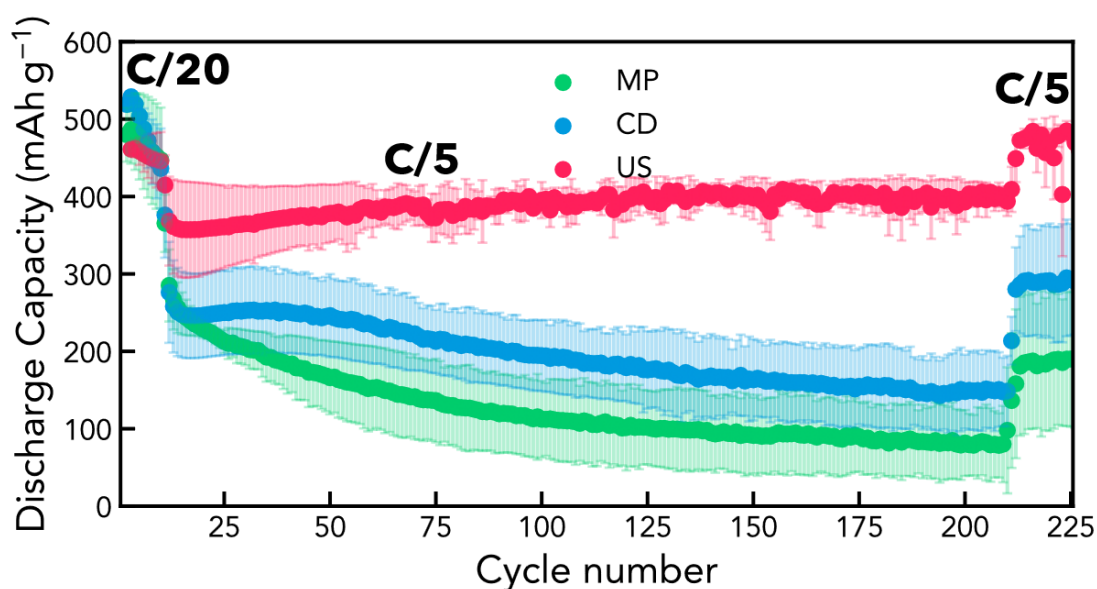


**Figure S10. Cycling of different Composites** Average discharge capacity as a function of cycle number for different FeF<sub>2</sub> composites. The rate was changed after 10 cycles from C/20 to C/5 and then back to C/20 at cycle number 210. Three different composites are compared, mortar and pestle (MP), co-dispersion (CD), and ultra-sonication (US).



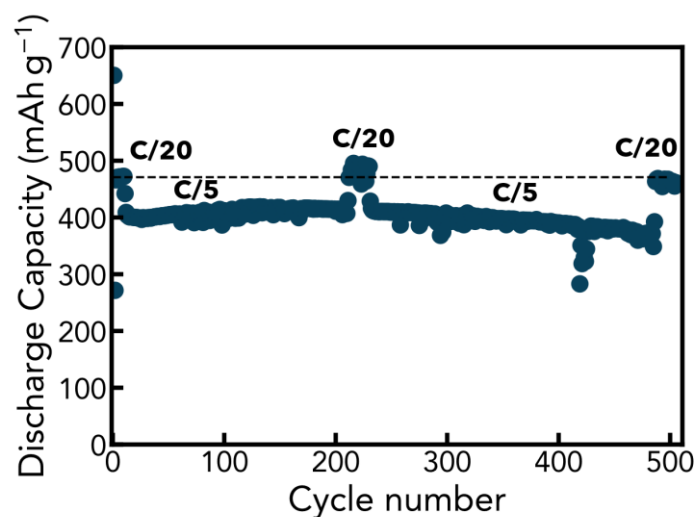


**Figure S11. Cycling of Ultra-stirred Composite** Discharge capacity as a function of cycle number for US cathodes with an active material content of 70 wt%.

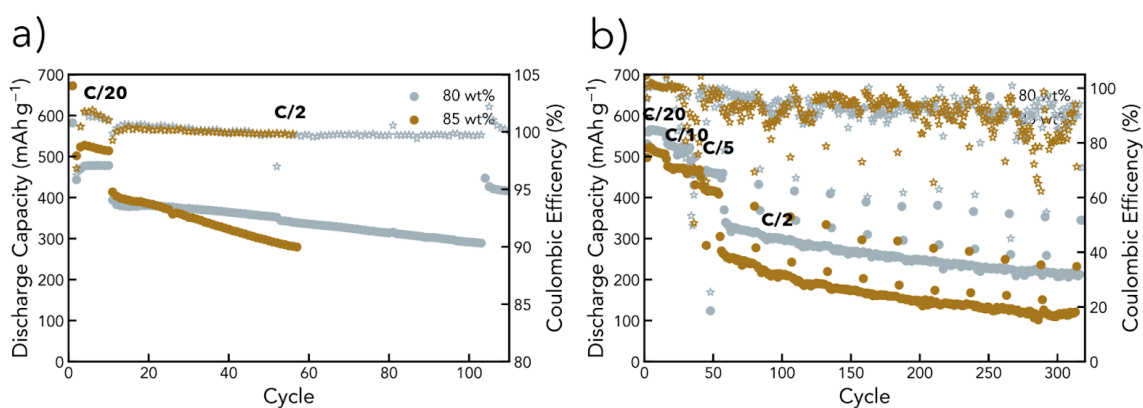


**Figure S12. High Active Material Content Cycling** Discharge capacity as a function of cycle number of ultra-stirred FeF<sub>2</sub> cathodes with an active material content of 80 wt% and 85 wt%. a) Shows a C/20 cycling rate in the first ten cycles and then an asymmetric cycling profile with a C/2 discharge rate and a C/20 charge rate. b) rate capability test where a C/20, C/10, C/5, and C/2 rate was applied during both dis- and recharge.

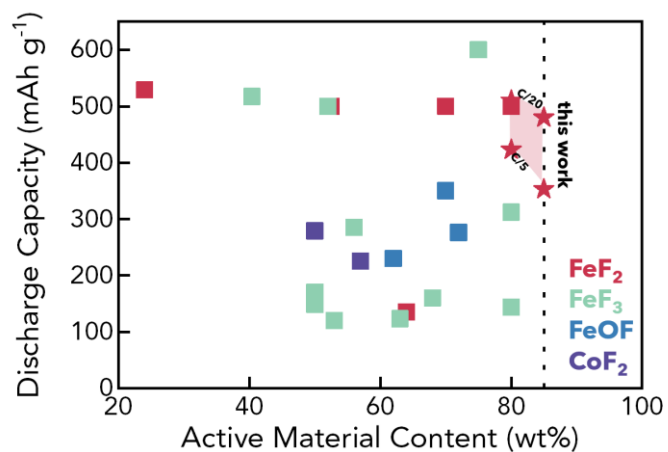


**Figure S13. Literature Comparison** Literature comparison of TMF cathodes. The plot shows the retained discharge capacity as a function of its active material content.<sup>1-27</sup>

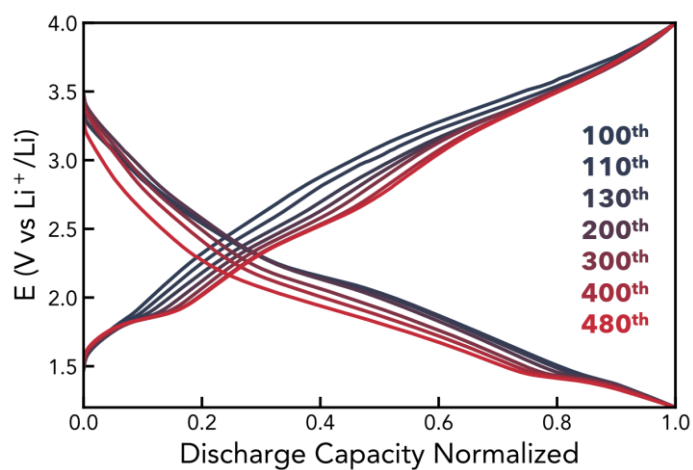


**Figure S14. Normalized GCPL** Normalized GCPL at different cycle numbers of the US FeF<sub>2</sub> cell shown in Figure S17.

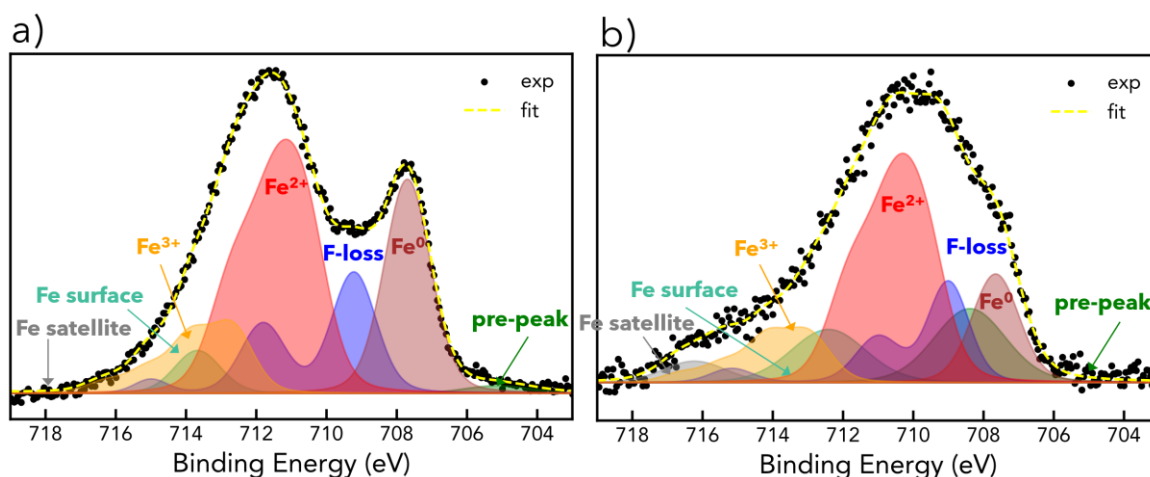


**Figure S15. Iron XPS of cycled cathodes** XPS fit in the iron energy range for two different US cathodes. a) corresponds to a cathode after the second cycle and b) was fitted to the cathode cycled 505 times. The measurements were collected after 3600s of argon sputtering. All fits were set up using constraints for peak splitting and FWHM extracted from Grosvenor et al.<sup>28</sup>

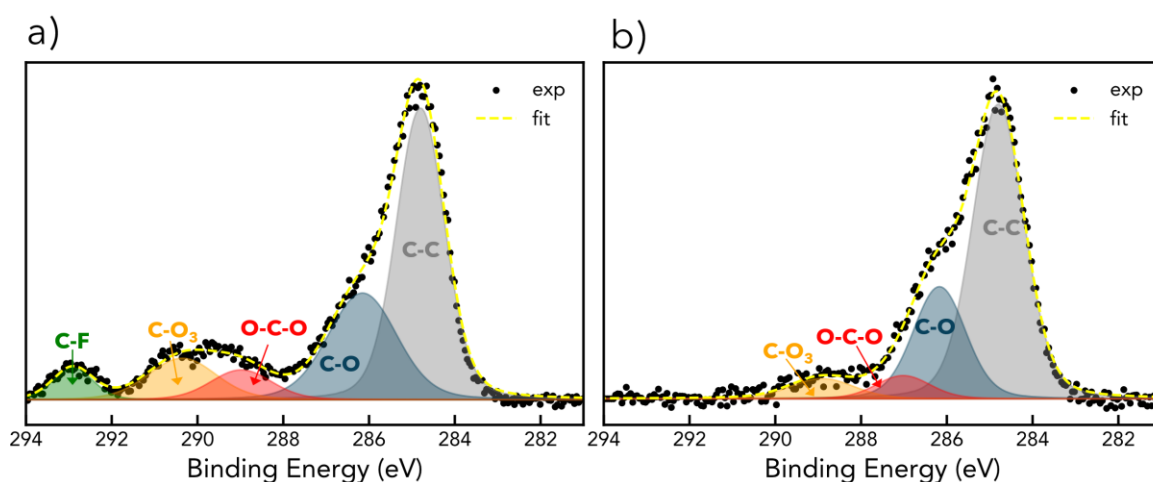


**Figure S16. Carbon XPS of Cycled Cathodes** XPS fit in the carbon energy range for two different US cathodes. a) corresponds to a cathode after the second cycle and b) was fitted to the cathode cycled 505 times. The measurements were conducted without any argon sputtering to preserve the cathode's CEI.

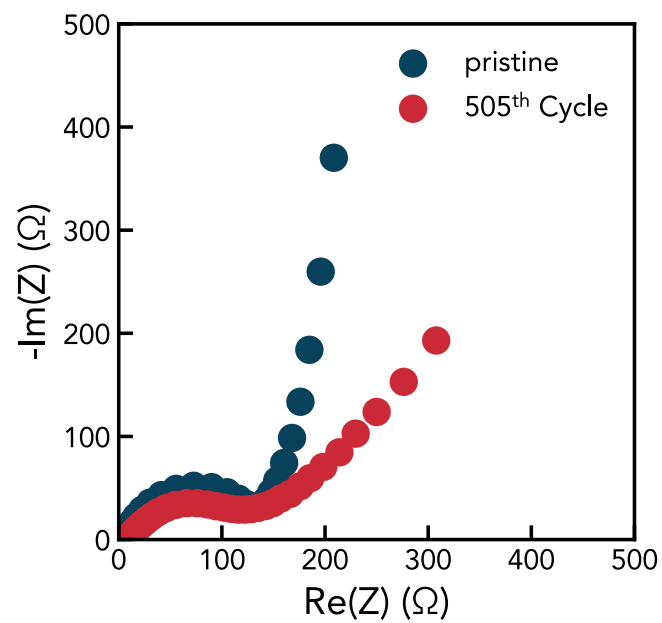


**Figure S17. EIS** Impedance of the US cathode before and after cycling.

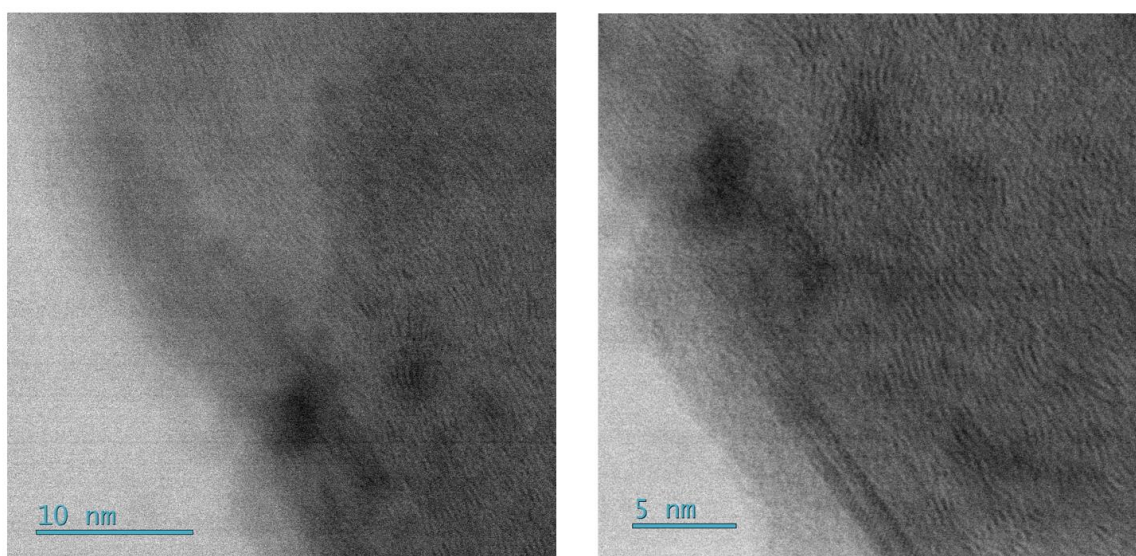


**Figure S18. Post Cycling STEM** Post mortem STEM of US cathodes after 500 cycles.

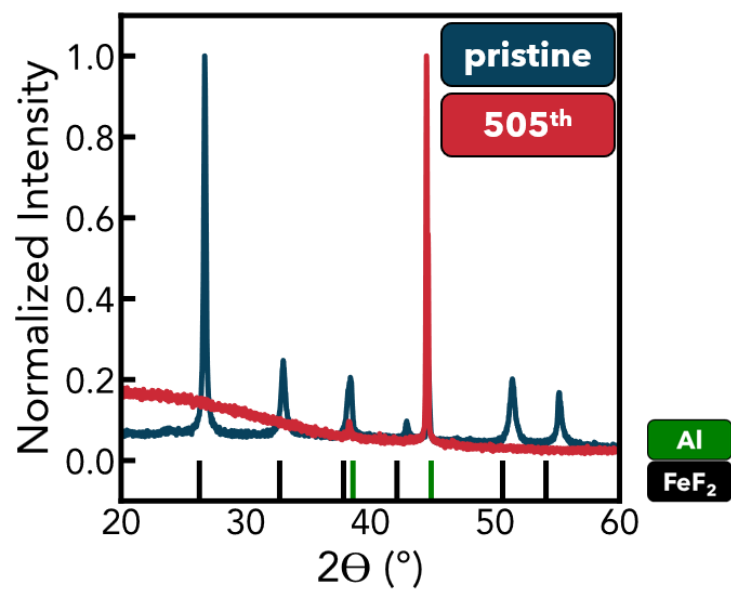


**Figure S19. Post-cycling XRD** XRD pattern of a disassembled US cathode cycled twice and 505 times at 30°C. The reference spectrum of FeF<sub>2</sub> and aluminium are inserted.

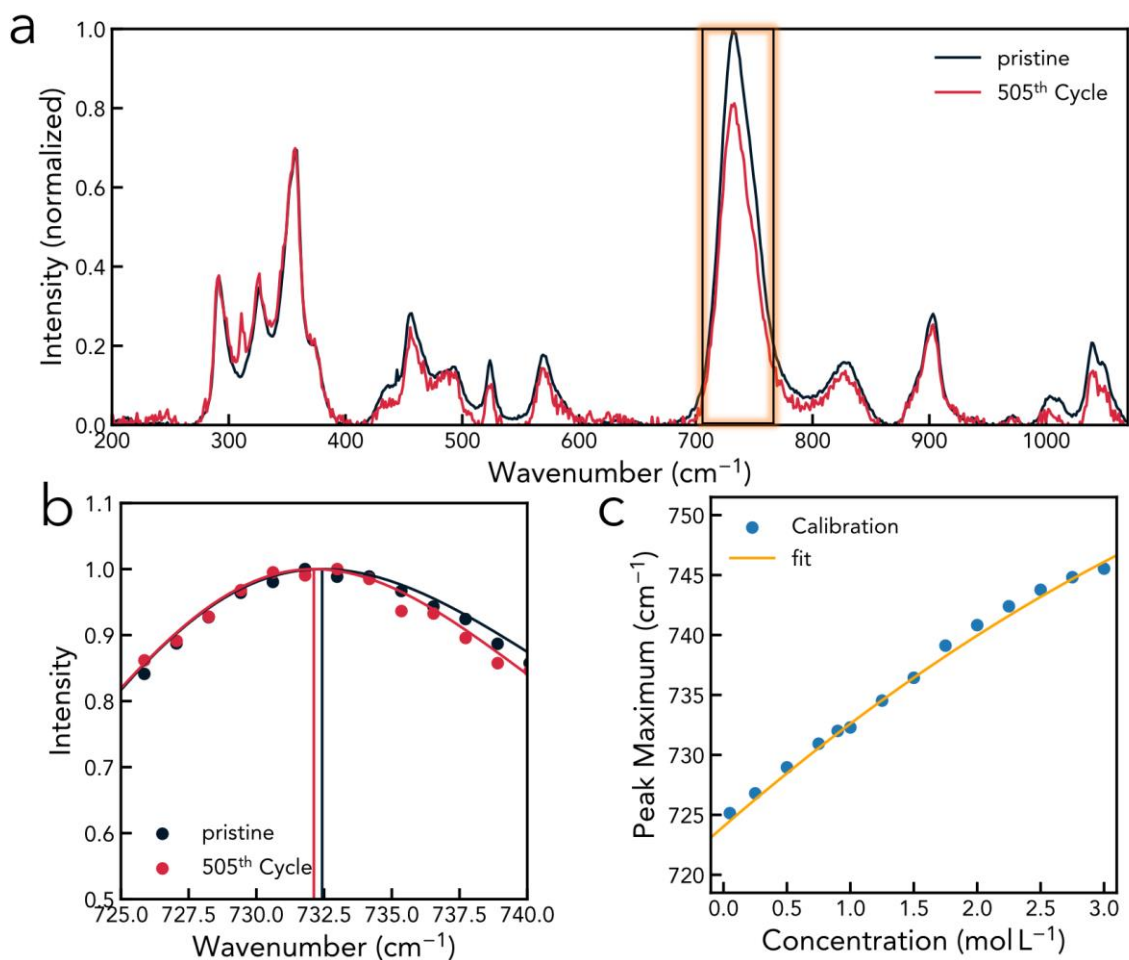


**Figure S20. Quantification of FSI<sup>-</sup> consumption** Determination of LiFSI concentration in Pyr<sub>1,3</sub>FSI ionic liquid electrolyte was inspired by an earlier study where LiFSI concentration were visualized in operando Raman measurements.<sup>29</sup> In short, the S–N–S bending mode, at 730 cm<sup>-1</sup> peak shifts to higher wavenumbers monotonically with increasing lithium concentration because of the continuing formation of high-energy bonding Li(FSI)<sub>2</sub>–structures. Therefore, the peak maximum can be used to calculate the LiFSI concentration in the electrolyte. As shown in Figure SI15a and SI15b, the peak maximum of the cell cycled 505 times shifts to lower wave numbers. A calibration line to convert the peak maximum to a concentration was obtained by measuring 14 different LiFSI in Pyr<sub>1,3</sub>FSI concentrations as shown in b).

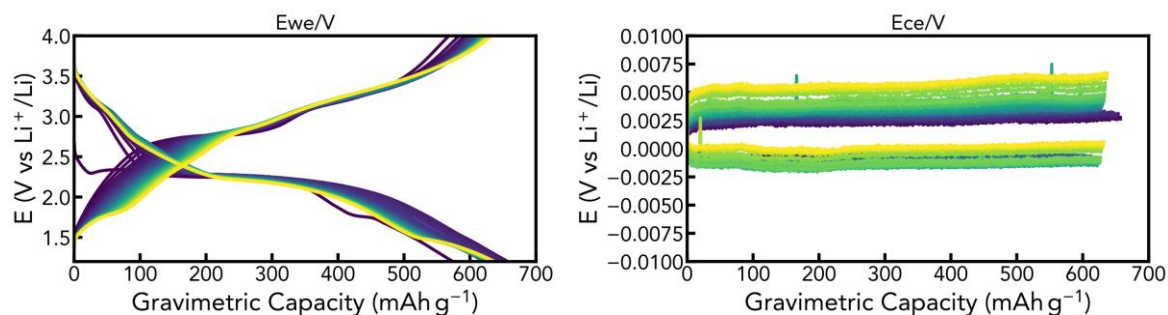


**Figure S21. Three Electrode Cell Cycling at 80°C** Working electrode potential and counter electrode potential of a three-electrode cell (US cathode  $\text{FeF}_2$ :1M LiFSI Pyr<sub>1,3</sub>FSI lithium metal vs lithium metal) for 50 cycles at 80°C. Cycle number increases from dark to bright.

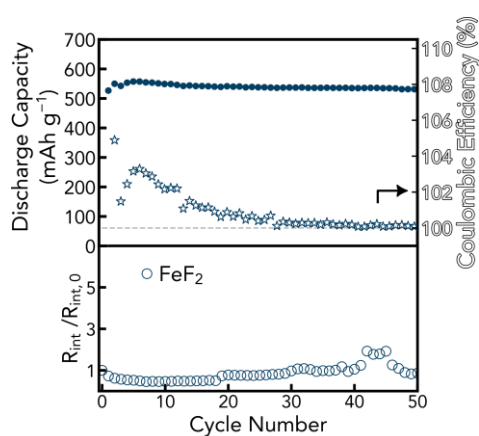


**Figure S22. Three Electrode Cell Cycling at 30°C** Discharge capacity of three-electrode cells cycling  $\text{FeF}_2$ -IL at 30°C at a C/20 rate. Below is the corresponding cathode interphase impedances as a function of cycle number determined by EIS.

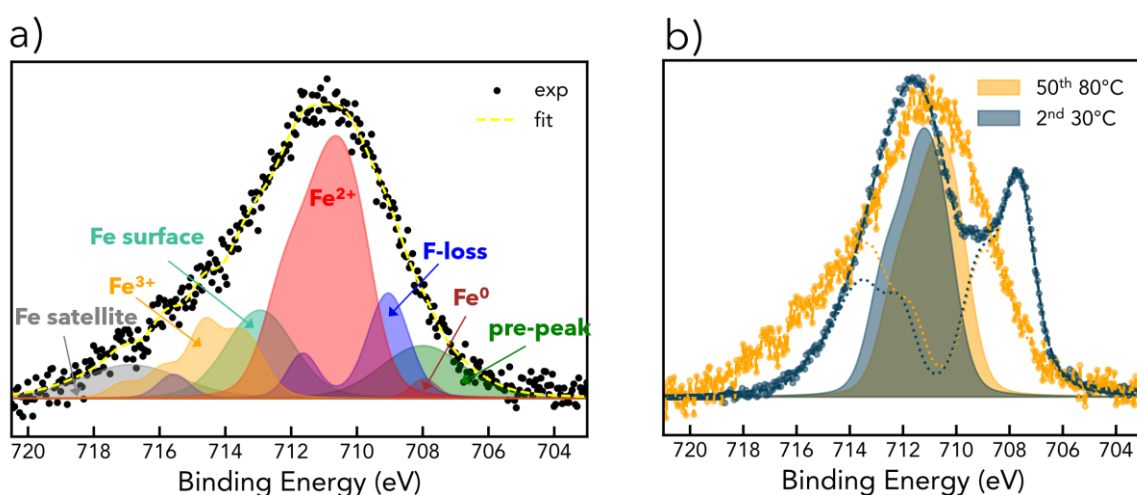


**Figure S23. Post-cycling XPS** a) XPS fit in the iron energy range for a cathode cycled 50 times at 80°C after 3600s of argon sputter. The metallic iron peak was set at the same energy and FWHM values as observed before ( $707.7 \pm 2$  eV;  $1.5 \pm 0.2$ ) in Figure S15. b) shows a comparison with a cathode cycled two times at 30°C.



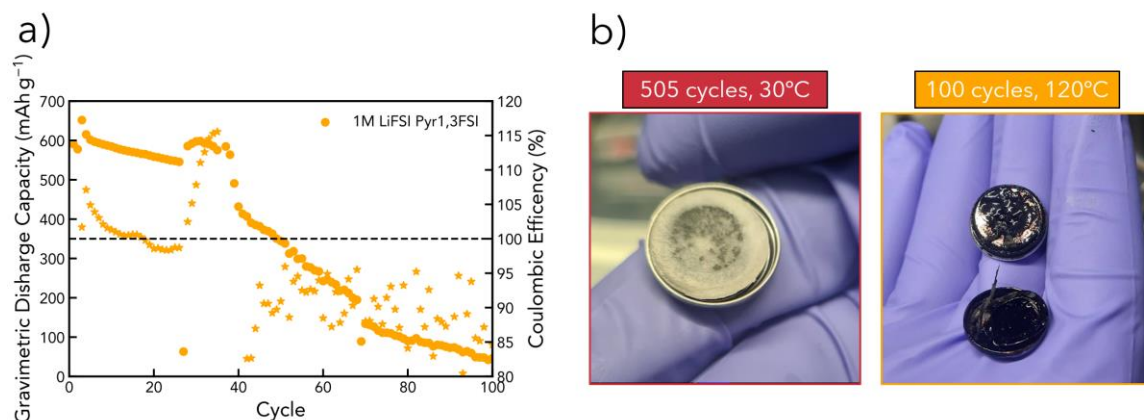


**Figure S24. Cycling at 120°C** a) Discharge capacity as a function of cycle number in a coin cell cycling at 120°C. b) shows the disintegrated cells cycled at 30°C and 120°C respectively. The cell cycled at 120°C shows disintegration of the composite, indicating the PVDF binder is not stable enough for continuous operation at such a high temperature.

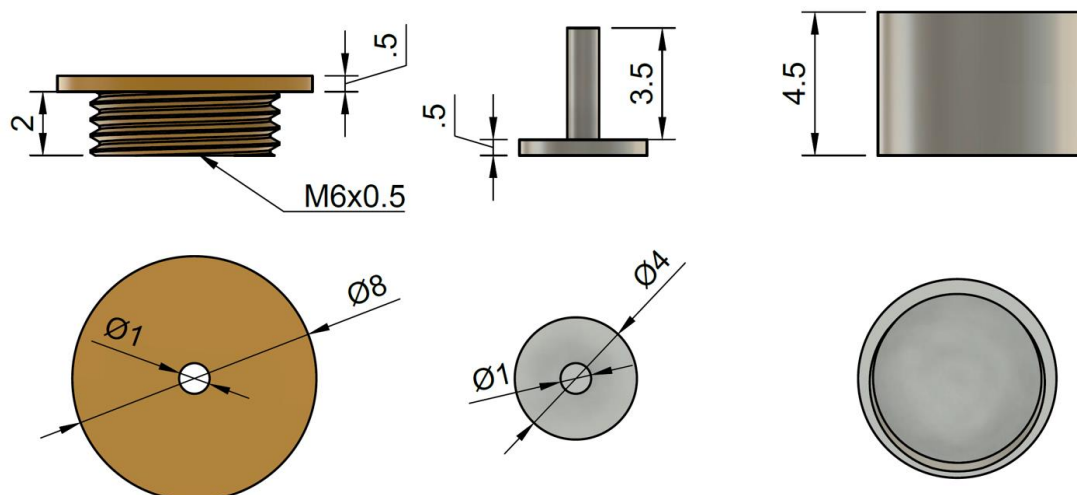


**Figure S25. Design of in-situ STA Cell** Electric flight applications require batteries with improved cell safety features due to the critical nature of operation failures. Consequently, we investigated the thermal stability of the proposed cell chemistry individually and in a full-cell configuration. The full configuration allows monitoring of the heat flow of any reaction within the battery, including the ones originating from the liquid-solid interphases. Therefore, we designed a tailor-made battery casing (STA-cell) that was suitable to be mounted into an STA setup.

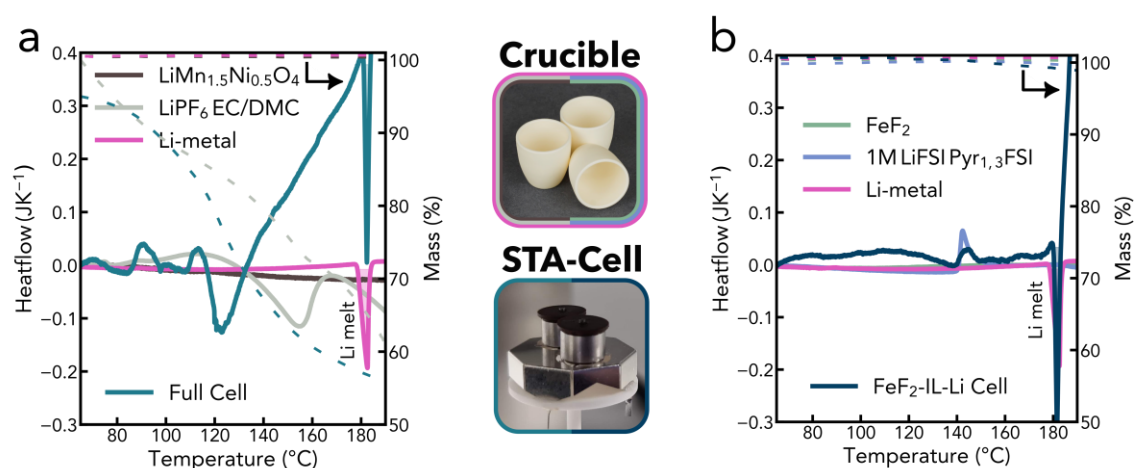


**Figure S26. Cell Safety Comparison** To account for the formation of a CEI and SEI, the STA-cell was dis- and recharged, before its investigation on the STA. The observed heat flow was calibrated by the endothermic lithium melting peak and plotted over the individual cell components. Before testing the STA-cell, all active cell components were characterised in a conventional alumina crucible. For comparison, an identical thermal analysis of a conventional layered-oxide in organic, LNMO in LP30, 1M LiPF<sub>6</sub> in ethylene carbonate : dimethyl carbonate 1:1 cell was conducted (Figure SI20b). The STA-cell, containing all active components and both electrode-electrolyte interphases, shows additional heat flow peaks and a significant exothermic drift from 140 °C up to the melting point of lithium. This indicates thermally induced electrode interphase reactions and serves as a proof-of-concept to monitor heat flow in the STA-cell.

Next, the FeF<sub>2</sub>-IL-lithium metal chemistry was investigated. Similar to before, all components were individually measured in a crucible as shown in Figure SI20b. Neither of the three components displays any mass loss within the investigated temperature range. Differential scanning calorimetry (DSC) of the IL shows one exothermic peak at around 140°C. LiFSI melts at a similar temperature range as indicated by the endothermic melting peak of the pure salt. Consequently, the exothermic peak observed in the IL might originate from a structural reorganization of the Li<sup>+</sup>-FSI<sup>-</sup> ions. Besides, only a lithium melting peak is visible amongst the active cell components.

The STA-cell exhibited the same exothermic peak that was visible when measuring the pure electrolyte. The small exothermic drift observed between 80-140°C is attributed to minor differences in the sample and reference STA-cell. No additional peaks were detected which indicates the full cell, including its interphases, is stable to at least 140°C. The results indicate that no thermal runaway occurs up to the melting point of lithium metal. However, additional accelerating rate calorimeter (ARC) measurements in larger cell formats are required for verification.

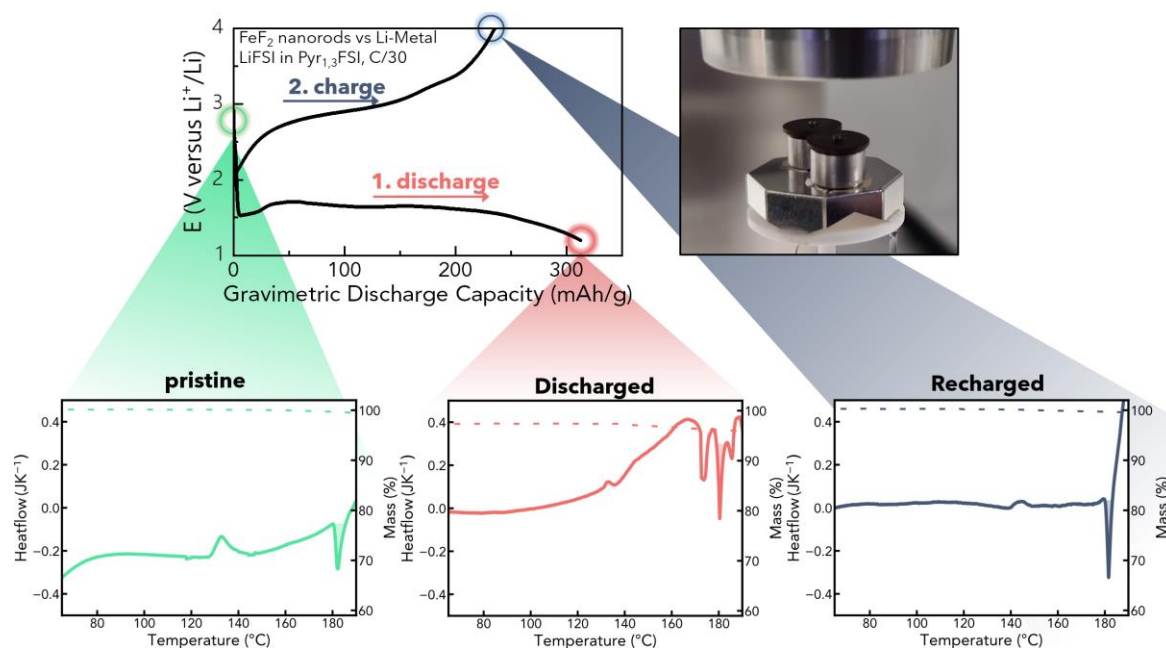


**Figure S27. Cell Safety Comparison different SOC** The experiment was repeated at different states of charge (SOC). No heat flow could be detected below the exothermic peak at  $140^{\circ}\text{C}$ . However, an exothermic drift was observed in the discharged cell, which could be attributed to electrolyte decomposition catalyzed by iron metal covering the surface of the discharge cathode. This is an interesting finding as it suggests the thermal stability of the cells decreases with SOC, which is contrary to most cell chemistries.

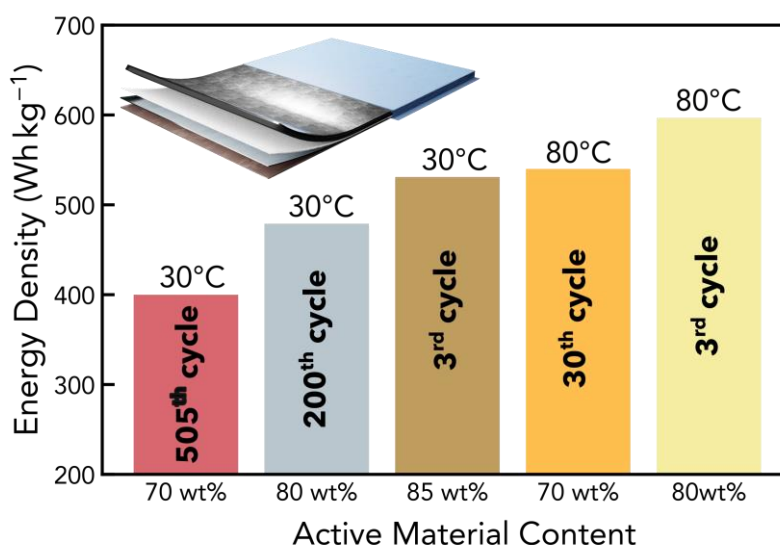


**Figure S28. Energy Densities** The cell level energy densities were calculated using the cycling data showcased in the manuscript. In addition, some parameters were approximated based on industry standards and marked orange in the table S1. The most important assumptions made are that the capacity retention, described in the manuscript from coin cell cycling data, can be maintained under higher cathode loadings of  $39 \text{ mg/cm}^2$  and in lean electrolyte conditions of  $0.03 \text{ mL/g}$ .

**Table S1:** Parameters used to calculate energy densities in Figure S28**Cathode**

Composition	Active material	FeF <sub>2</sub>	70wt%
	Carbon additive	Super-P	20wt%
	Binder	PVDF	10wt%
Density	Active material	FeF <sub>2</sub>	4.09 g/cm <sup>3</sup>
	Carbon additive	Super-P	2.1 g/cm <sup>3</sup>
	Binder	PVDF	1.78g/cm <sup>3</sup>
	Current collector	Al	2.7 g/cm <sup>3</sup>
Cathode layer	Porosity		30%
	Cathode density		2.17 g/cm <sup>3</sup>
	Double side coating thickness (excluding current collector)		359.4 $\mu\text{m}$
	Thickness of current collector	Al	20 $\mu\text{m}$
A/C ratio			1.05
Cathode electrode	Loading(One side)		39mg/cm <sup>2</sup>
	Discharge capacity		461mAh/g
	Charge capacity		461 mAh/g
	Areal discharge capacity		12 mAh/cm <sup>2</sup>

**Anode**

Composition	Active material	Li metal	100 wt%
Material density	Active material	Li metal	0.534 g/cm <sup>3</sup>
	Current collector	Cu	8.96 g/cm <sup>3</sup>
Anode layer	Porosity		0%
	Electrode density		0.534 g/cm <sup>3</sup>
	Double side coating thickness (excluding current collector)		64.1 $\mu\text{m}$
	Thickness of current collector	Cu	10 $\mu\text{m}$
Anode electrode	Loading (One side)		3.42 mg/cm <sup>2</sup>

## Separator

Separator		Celgard	100wt%
Material density		Celgard	1 g/cm <sup>3</sup>
Separator layer	Porosity		30
	Layer density		0.70 g/cm <sup>3</sup>
	Thickness		30 μm

## Electrolyte

Electrolyte	Material	1M LiFSI Pyr13FSI	100 wt%
	Density		1.4 g/cm <sup>3</sup>

## Cell Design

Cathode side	Double layer	Number	34
	Current collector	Length	161.5 mm
		Width	121.5 mm
	Margin (Current collector-coated area)	Length direction	4.0 mm
		Width direction	4.0 mm
	Coated area	Length	157.5 mm
		Width	117.5 mm
	Margin (Laminate outer-current collector)	Length direction	38.5 mm
		Width direction	8.5 mm
Anode	Double layer	Number	33
	One side	Number	2
	Current collector	Length	161.5 mm
		Width	121.5 mm
	Margin (Current collector-coated area)	Length direction	2.0 mm
		Width direction	2.0 mm
	Coated area	Length	159.5 mm
		Width	119.5 mm
	Margin (Laminate outer-current collector)	Length direction	38.5 mm
		Width direction	8.5 mm
Separator		Number	68
		Length	161.5 mm
		Width	121.5 mm

## Cell Design

Outer laminate (Excluding tab)		Number	2
		Length	200.0 mm
		Width	130.0 mm
		Thickness (PET)	0.150 mm
Outer laminate (Including tab)		Number	2
		Length	250.0 mm
		Width	170.0 mm
		Thickness (PET)	0.148 mm
	Laminate	Density	205 g/m <sup>2</sup>
Tab		Length	50.00 mm
		Width	40.0 mm
	Cathode side	Thickness	0.2 mm
		Density	2.7 g/cm <sup>3</sup>
	Anode side	Thickness	0.2 mm
		Density	9.0 g/cm <sup>3</sup>

## Cell Level

Total Cell Weight	790.3 g
Cell Capacity	158.4 Ah
Average Cell Potential	2.0 V
Cell Energy Density (vol)	684.7 Wh/L
Cell Energy Density (grav)	400.3 Wh/kg

## References

1. Huang, Q., Turcheniuk, K., Ren, X., Magasinski, A., Gordon, D., Bensalah, N., and Yushin, G. (2019). *Advanced Energy Materials* 9, 1.
2. Song, H., Cui, H., and Wang, C. (2015). *Journal of Materials Chemistry A* 3, 22377.
3. Xiao, A. W., Lee, H. J., Capone, I., Robertson, A., Wi, T. U., Fawdon, J., Wheeler, S., Lee, H. W., Grobert, N., and Pasta, M. (2020). *Nature Materials* 19, 644.
4. Huang, Q., Turcheniuk, K., Ren, X., Magasinski, A., Song, A. Y., Xiao, Y., Kim, D., and Yushin, G. (2019). *Nature Materials* 18, 1343.
5. Kim, S., Liu, J., Sun, K., Wang, J., Dillon, S. J., and Braun, P. V. (2017). *Advanced Functional Materials* 27, 1.
6. Gu, W., Magasinski, A., Zdyrko, B., and Yushin, G. (2015). *Advanced Energy Materials* 5, 1.
7. Su, Y., Chen, J., Li, H., Sun, H., Yang, T., Liu, Q., Ichikawa, S., Zhang, X., Zhu, D., Zhao, J., Geng, L., Guo, B., Du, C., Dai, Q., Wang, Z., Li, X., Ye, H., Guo, Y., Li, Y., Yao, J., Yan, J., Luo, Y., Qiu, H., Tang, Y., Zhang, L., Huang, Q., and Huang, J. (2022). *Advanced Science* 9, 1.
8. Sun, L., Li, Y., and Feng, W. (2023). *Small Methods* 7, 1.
9. Han, Y., Li, H., Li, J., Si, H., Zhu, W., and Qiu, X. (2016). *ACS Applied Materials and Interfaces* 8, 32869.
10. Fu, W., Zhao, E., Sun, Z., Ren, X., Magasinski, A., and Yushin, G. (2018). *Advanced Functional Materials* 28, 1.
11. Wu, W., Wang, S., Wu, W., Chen, K., Hong, S., and Lai, Y. (2019). *Energy Conversion and Management* 182, 262.
12. Zhang, Q., Zhang, Y., Yin, Y., Fan, L., and Zhang, N. (2020). *Journal of Power Sources* 447, 227303.
13. Guntlin, C. P., Zünd, T., Kravchyk, K. V., Wörle, M., Bodnarchuk, M. I., and Kovalenko, M. V. (2017). *Journal of Materials Chemistry A* 5, 7383.
14. Liu, M., Wang, Q., Chen, B., Lei, H., Liu, L., Wu, C., Wang, X., and Yang, Z. (2020). *ACS Sustainable Chemistry and Engineering* 8, 15651.
15. Tan, J., Liu, L., Hu, H., Yang, Z., Guo, H., Wei, Q., Yi, X., Yan, Z., Zhou, Q., Huang, Z., Shu, H., Yang, X., and Wang, X. (2014). *Journal of Power Sources* 251, 75.
16. Li, J., Xie, K., Lai, Y., Zhang, Z., Li, F., Hao, X., Chen, X., and Liu, Y. (2010). *Journal of Power Sources* 195, 5344.
17. Chu, Q., Xing, Z., Tian, J., Ren, X., Asiri, A. M., Al-Youbi, A. O., Alamry, K. A., and Sun, X. (2013). *Journal of Power Sources* 236, 188.
18. Wang, Q., Zhao, C., Wang, J., Yao, Z., Wang, S., Kumar, S. G. H., Ganapathy, S., Eustace, S., Bai, X., Li, B., and Wagemaker, M. (2023). *Nature Communications* 14, 440.
19. Guan, T., Zhao, L., Zhou, Y., Qiu, X., Wu, J., Wu, G., and Bao, N. (2023). *Advanced Energy Materials* 2301680, 1.
20. Fan, X., Hu, E., Ji, X., Zhu, Y., Han, F., Hwang, S., Liu, J., Bak, S., Ma, Z., Gao, T., Liou, S. C., Bai, J., Yang, X. Q., Mo, Y., Xu, K., Su, D., and Wang, C. (2018). *Nature Communications* 9, 1.
21. Li, W., Chen, Y., Zangiabadi, A., Li, Z., Xiao, X., Huang, W., Cheng, Q., Lou, S., Zhang, H., Cao, A., Roy, X., and Yang, Y. (2020). *ACS Applied Materials and Interfaces* 12, 33803.
22. Zhai, J., Lei, Z., and Sun, K. (2019). *Chemistry - A European Journal* 25, 7733.
23. Li, X., Zhang, Y., Meng, Y., Wang, Y., Tan, G., Yuan, H., and Xiao, D. (2019). *Inorganic Chemistry Frontiers* 6, 465.



24. Ju, L., Wang, G., Liang, K., Wang, M., Sterbinsky, G. E., Feng, Z., and Yang, Y. (2020). *Advanced Energy Materials* 10, 1.
25. Fan, X., Luo, C., Lamb, J., Zhu, Y., Xu, K., and Wang, C. (2015). *Nano Letters* 15, 7650.
26. Wu, F., Srot, V., Chen, S., Zhang, M., Van Aken, P. A., Wang, Y., Maier, J., and Yu, Y. (2021). *ACS Nano*, 10.1021/acsnano.0c08918.
27. Wang, L., He, M., Hu, Y., Zhang, Y., Liu, X., and Wang, G. (2015). *Energy* 82, 229.
28. Grosvenor, A. P., Kobe, B. A., Biesinger, M. C., and McIntyre, N. S. (2004). *Surface and Interface Analysis* 36, 1564.
29. Fawdon, J., Ihli, J., Mantia, F. L., and Pasta, M. (2021). *Nature Communications* 12, 10.1038/s41467-021-24297-0.